Synthesis and Characterization of ZIF based CeO_2 and Cu doped CeO_2 catalysts

By

Shabahat Bibi

School of Chemical and Materials Engineering
National University of Sciences and Technology
2019

Synthesis and Characterization of ZIF based CeO_2 and Cu doped CeO_2 catalysts

Name: Shabahat Bibi

Reg No.: 00000171333

This work is submitted as an MS thesis in partial fulfilment of the requirement for the degree of

MS in Chemical Engineering

Supervisor Name: Dr. Erum Pervaiz

School of Chemical and Materials Engineering (SCME)

National University of Sciences and Technology (NUST)

H-12 Islamabad, Pakistan

2019

Dedication

To my family and friends

ACKNOWLEDGEMENTS

All praise to Allah Almighty who is the most beneficent and merciful. I would like to appreciate and express my sincere gratitude to my research supervisor**, Dr. Erum Pervaiz** for her support, supervision and kind guidance to lead me in the right direction whenever I needed it. I would also like to acknowledge my gratitude to committee members, **Dr. Sarah Farrukh** and **Dr. M. Bilal Khan Niazi** for their helpful suggestions and guidance. In the end, I must express my deep gratitude to my parents for bestowing me with constant support and endless encouragement throughout my years of study and through the process of researching and writing this thesis. This accomplishment would not have been possible without them.

Shabahat Bibi

ABSTRACT

Catalysts capable of achieving high performance without compromising the green credentials are a pre-requisite for the development of a sustainable process. Recently, ZIF-67 have gained immense interest in the field of catalysis due to their high thermal and chemical stability and exceptional functionalities. In our study, a hybrid of CeO_2 nanoparticles with ZIF-67 is synthesized by embedding the ceria nanoparticles into the microporous structure of ZIF-67 through a facile technique. It is then employed for the oxidation of cyclohexene into adipic acid as an alternative to expensive noble metal-based catalysts. The heterogeneous ZIF-67/CeO_2 catalyst was found catalytically active towards the oxidation of cyclohexene with nearly complete conversion into adipic acid, under moderate and co-catalyst free reaction conditions. On the other hand, Cu doped CeO_2 nanospheres have been prepared by a facile hydrothermal route. A performance comparison of MOF embedded CeO_2 nanoparticles with its metal doped structure is presented, with an adequate understanding of ceria's enhanced catalytic and reducible properties. The as-prepared CeO_2/ZIF-67 hybrid comprehend the advantage of a microporous manner depicted by the MOF matrix combined with the effective functional characteristics of cerium oxide's nanoparticles.

Table of Contents

LIST OF FIGURES

LIST OF TABLES

ABBREVIATIONS

TEM	Transmission Electron Microscopy
PVP	Polyvinyl Pyrrolidone
OSC	Oxygen Storage Capacity
OVD	Oxygen Vacancy Defects
ZIF	Zeolitic Imidazolate Framework
MOFs	Metal Organic Frameworks
FCC	Face-Centered Cubic
XRD	X-ray Diffraction
SEM	Scanning Electron Microscopy
FTIR	Fourier Transform Infrared Spectroscopy
TG/DTA	Thermogravimetric/Differential Thermal Analyzer
XPS	X-ray Photoelectron Spectroscopy
TPR	Temperature Programmed Reduction
AA	Adipic Acid

CHAPTER 1

Introduction

1.1 Cerium Oxide

1.1.1 General Background of Cerium Oxide

Cerium belongs to the lanthanide series in the periodic table and is one of the most plentiful rare earth elements. The title "rare earths" represents 17 chemically alike metal elements consisting of yttrium, scandium, and the lanthanide series, which were discovered over a period of almost 160 years [1]. Cerium has the atomic number of 58 and it occurs in earth's crust even more abundantly than metals like lead and copper, with a concentration of 66.5ppmpublished by Lide in 1997 [2]. The electrons of cerium are placed in the configuration [Xe] $4f^1 5d^1 6s^2$, of which the four external electrons are valence electrons. Cerium displays oxidation states of 4+ and 3+ and is considered an exception because of an empty stable f-shell in Ce^{+4} [3]. Cerium is found to be unstable in an oxygen environment and forms either CeO_2 or Ce_2O_3, depending on the temperature and oxygen pressure [4]. The dioxide (CeO_2), also known as ceria, has a fluorite structure, a face-centered cubic unit cell with space group Fm-3m. The lattice parameter in every unit of cerium is 5 Å, and oxygen-oxygen distance is 2.705 Å, which is half the value of lattice parameter. In the structure of CeO_2, each cerium cation, at the corner of the cube, is enfolded by eight oxygen anions and each oxygen anion is tetrahedrally bounded by four cerium cations. If the structure is enlarged by putting cubic units of oxygen at each corner, it will result into a detailed display of an eight-fold cubic arrangement of each cerium, that fill the center of the cube in an alternate manner. Its structure is shown in Fig.1.

This aspect of ceria demonstrates the fact that there are large empty octahedral holes in its structure, a character that is important in the applications of ceria, due to the defect structure, and will be discussed in detail in later sections. Ce_2O_3, another oxide of cerium, is identified as unstable towards oxidation and gets oxidized as the pressure reaches up to 10^{-40} atm of oxygen, that's when CeO_2 begins to form [4]. CeO_2 is one of the reducible

oxides where it is easy for them to lose electrons or oxygen. This inherent property of ceria reflects in its ability to be an efficient catalyst in automobile exhausts emission control or solid oxide fuel cells. And it could be enhanced by doping of ceria with foreign cations [5].

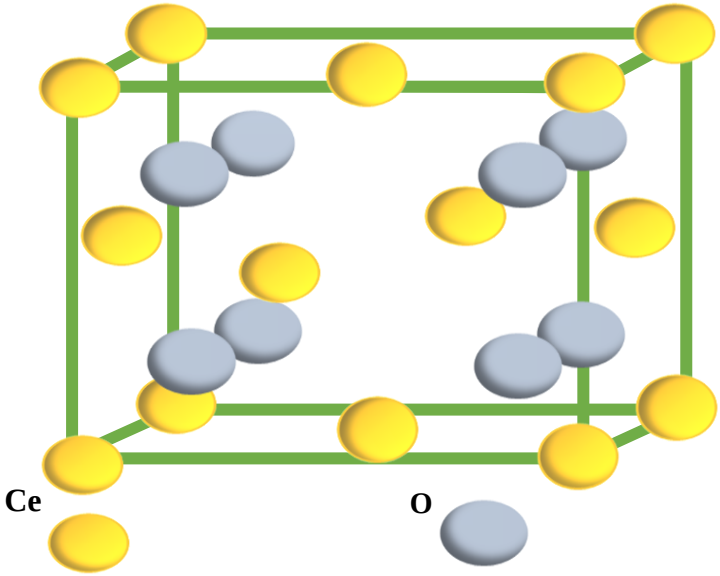

Figure 1 Atomic structure of unit cell of CeO_2

1.1.2 Morphology

Ceria has been produced in different morphological nanostructures, such as, rods, tubes, which are reported to directly affect its surface properties because of the different crystal planes it exposes. It depends upon the specific synthesis procedures used for their production, and sometimes the addition of a surfactant could be the crucial factor in determining the shape of the crystal. For example, in the synthesis of ceria nanocubes, TEM results have shown the 100 plane to be the dominant plane. It has high surface energy which is preferred for their better catalytic performance. It can be attained by using a surfactant like PVP, or tetramethyl ammonium hydroxide [6, 7].

Ceria nanorods have been reported to have superior activities than other morphological structures of ceria in numerous reactions like CO oxidation, NO elimination etc [8, 9]. It exposes the 111 plane, although in some reports, 100 and 110 planes have been shown. It has higher OSC due to greater portion of more responsive100 and110 planes [10]. Octahedrons of ceria exposes the 111 plane but it has exhibited the slowest catalytic response in comparison to ceria's other morphological structures [11]. Other shapes

include nanosheets, spindles, and tubes etc. Several synthesis processes have been developed to achieve these desired uniform shapes of the ceria's nanocrystal, however it is a still a challenge to achieve well controllable and invariable crystal size because of their unique shapes [12].

1.1.3 Synthesis of Ceria

Ceria nanostructured materials tend to have separate physiochemical properties than its bulk analogue. This is because of their very minute sizes, higher concentration of OVD's, and enhanced surface areas [4]. Generally, the synthesis procedures of ceria nanocrystals could be divided into physical and chemical methods. The two usual and most widespread chemical methods are called hydrothermal and co-precipitation, whereas ball milling is an important physical procedure [13].

1.1.3.1 Hydrothermal Method

In a hydrothermal process, cerium's oxide and its crystalline growth occurs in an aqueous solution at elevated temperature and pressure in a tightly closed container, which is called an autoclave. This process is among the most significant and well-developed processes for ceria's synthesis and holds some really great advantages. These include the reaction temperature being less than the melting point of the materials taking part in the reaction, and the operative parameters like temperature, time interval, or the autoclave kinds can be easily adjusted to alter the reactivities of the resultant oxide [4].

1.1.3.2 Co-Precipitation Method

In a co-precipitation method, two salt precursors, dissolved in aqueous solutions, are needed which are then combined together to get the product after reaching a certain value of pH. One of the precursors is a cerium salt, which could be Ce $(NO_3)_3.2H_2O$, $CeCl_3$, or $(NH_4)_2Ce(NO_3)_6$, etc., and the other one is a precipitating agent like NaOH, oxalic acid, NH_4OH, etc., [4]. It is a quick and facile synthesis procedure and also easy in managing the particle's dimension and composition [14].

1.1.4 Oxygen Vacancy Defect

Cerium oxide is known to have inherent defects or distortions in its lattice structure. These could generally be formed due to alternate presence and absence of cerium cations in its

respective lattice site. It could also be generated as a result of reactions with the surroundings or a solid [4]. The most common defect found in ceria is the oxygen vacancy defect, which is also known as its oxygen storage capacity. It is created when an oxygen ion or an atom leaves its original place and occupy a nearby location. It is ordinarily in lower concentration but it could be increased in a reducing environment where there's a stoichiometric change as well from CeO_2 to CeO_{2-x}. This happens due to the inherent capability of ceria to change its oxidation states from +4 to +3, owing to the lower energy d-orbital present in ceria. This aspect is very important for ceria as an industrial catalyst. It makes ceria to reserve oxygen in an oxygen rich environment and to release in oxygen lean environment [15].

1.1.5 Applications of Ceria

Ceria's applications in various fields like catalysis, electronics, ceramics, etc., owes to its prospective redox behavior between +4 and +3 oxidations, inherent bands energy in electronic configuration, and greater oxygen storage capacity [4].

1.2 Introduction to ZIF-67

ZIF67, with a sodomite topology, is an advanced form of MOFs, having a consistently porous and crystalline structure. Its structure is somewhat analogous to the regular aluminosilicates with superior thermal and chemical stabilities. The important character of ZIFs is to have combined advantages of both MOFs and zeolites [16].

1.2.1 Structure of ZIF-67

It is made out of Cobalt cation (Co^{+2}) and the organic compound (2-methylimidazole). The Co^{+2} groups, coordinated with 2-methyl imidazole linker, acts as the secondary building unit. Its structure has a cubical crystal symmetry and unit cell parameters are a=b=c=16.9589 Å as shown in Fig. 2 [17]. In their structure, the M (Co cation) components are crossed over by lm (imidazole linker) and the edge of M– lm– M is 145°. This structure is like that of Si– O– Si in regular silicon-based zeolites [18].

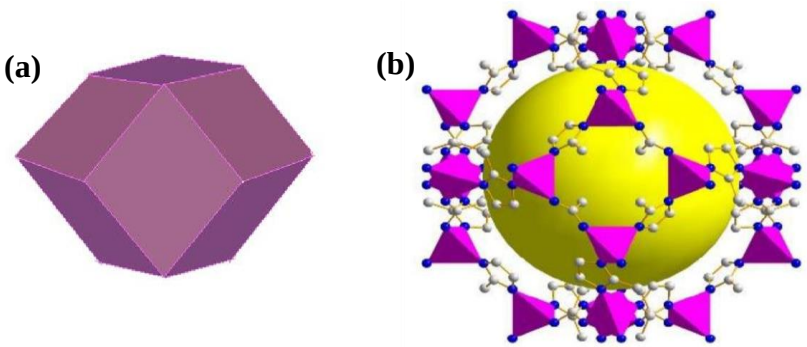

Figure 2 ZIF-67: (a) Rhombic dodecahedral morphology and (b) Crystal structure [17]

1.2.2 Synthesis of ZIF-67

ZIF-67 is typically prepared through hydrothermal and solvothermal techniques by using water or organic solvents with differing duration times from hours to days. It could also be prepared easily at room temperature by combining aqueous solutions of metal precursor and 2-methyl imidazole [19].

1.3 General Incorporation of functional nanoparticles inside MOF

MOFs are established crystalline and highly porous materials with distinct applications. However, to further enhance their functionalities and to achieve a synergistic impact in their respective applications, certain functional species could be inserted into their porous structures by carefully controlled strategies. This could be done either by inserting a pre-formed functional species into the MOF precursor solution or generating a hybrid structure of MOF-embedded nanoparticle by employing the MOF as a template [20]. ZIF-67 has been previously doped with Zn cation as a catalyst for CO_2 fixation. This resulted in an increased activity and selectivity of the catalyst because of the synergic influence of Co and Zn [21]. ZIF-67 has also been employed as a template, after embedding CeO_2 nanowires, for generating a CeO_2-Co_3O_4 hybrid structure having a polyhedral morphology [19]. Other examples of noble metals being inserted into MOFs are also reported but these are not economically viable [5].

This is a very attractive field for mixing functional ingredients like MOFs and metal/metal oxide nanoparticles to produce a solid synergic effect, in the fields of catalysis, electronics, as well as sensing. However, this area of research still faces some challenges

regarding the complete encapsulation of materials inside MOFs cavities, being able to regulate and maintain relevant properties of the encapsulated material, and therefore needs carefully controlled and well-developed synthesis strategies for their production.

1.4 Doping of Metal Oxides

Doping is generally defined as a science of modifying the intrinsic defects in a metal oxide crystal in order to enhance the catalytic, electrical, and optical properties of the host metal oxide. It is done by substituting a foreign metal cation; say a dopant D, into the host oxide that replaces the host metal cation, by specific chemical synthesis procedures. Now it could have the same valency as the host cation or smaller or greater valency in comparison to the displaced cation. In case of the same valency, the only changes that results from doping are a shift in size, or change in boundary orbitals resulted from the different bond strength between the dopant and oxygen. If the dopant D have a different valency, it leads to a rather complex situation in which charge irregularities occur, that must be countered by the generation of additional defects in the structure. Possibly all the metals from periodic table could serve as a dopant, but mostly transition metals are being doped into metal oxides. It greatly enhances the reducibility of the metal oxide and has been extensively studied for oxidation reactions for that matter [5].

1.5 Adipic Acid

Adipic acid (AA) is an important commercial organic compound, used primarily for the production of nylon 6,6. In addition, AA is extensively utilized in fertilizers, lubricants, paper, waxes and food industry [22, 23]. Its structure is shown in Fig. 3. Globally, the production of adipic acid exceeds 3.5 million metric tons with fast growing requirement of 4% annually [24]. Conventionally, AA is produced by the oxidation of cyclohexanol and cyclohexanone (so-called KA oil) with nitric acid (HNO_3), in majority industrial processes, in the presence of Copper (II) or Vanadium, as catalysts. Although, this process is economically viable but reduction of HNO_3 produces NO_X, as by-products.

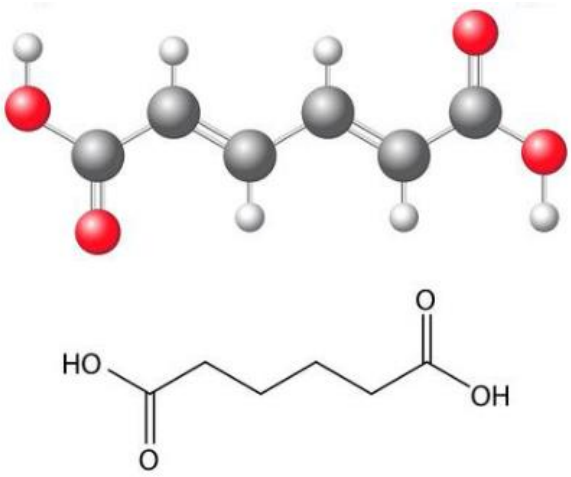

Figure 3 Structure of Adipic Acid [24]

Amongst them, NO and NO_2 are recycled back and N_2O_5 and N_2O are released in the atmosphere, thus adding to global warming and ozone depletion [25, 26]. Taking that into account, researchers have devoted their efforts in developing effective and environmentally friendly methods for industrial production of adipic acid that do not employ HNO_3 as oxidant. For that purpose, utilizing H_2O_2 and molecular oxygen as oxidant have been widely employed. H_2O_2 decomposes to water as a by-product and thus its application in producing adipic acid relates to establishing sustainable processes. However, its usage, in concentrations more than 60%, is intricate for safety reasons [27, 28]. On the other hand, scientists have also worked on the usage of renewable feedstock for the production of adipic acid, such as glucose, which is biologically converted into adipic acid by the use of microorganisms [29]. Even though, these processes are eco-friendly but prolonged reaction times and comparatively lower yields of adipic acid makes them not commercially viable. Noble metal-based catalysts have been reported to effectively catalyze the cyclohexene oxidation to adipic acid such as Pd, Rh, as well as Au [30-32]. Catalysts, alternative to noble metals, such as Ni supported on alumina, have also been synthesized for efficient conversion of cis,cis-muconic acid to adipic acid. These catalysts are viable as it exhibits almost the same performance as noble metal-based catalyst and at much lower cost [33].

1.6 Aim of Thesis

In our study, a performance comparison of MOF embedded CeO_2 nanoparticles with its metal doped structure are presented, with an adequate understanding of ceria's enhanced catalytic and reducible properties. For the MOF, we have chosen ZIF-67, due to its better thermal and chemical stability and dodecahedral morphology. On the other hand, Cu doped CeO_2 nanospheres have been prepared by a facile hydrothermal route. ZIF-67/CeO_2 is also utilized to effectively catalyze the production of adipic acid through oxidation of cyclohexene, under moderate reaction conditions.

CHAPTER 2

Literature Review

2.1 ZIF-67

2.1.1 ZIF-67 as a sacrificial template

Considering the dodecahedral morphology of ZIF-67, and the presence of Co cations, it has been used as a thermodissipitable template for the synthesis of various metal oxide or hydroxide catalysts. In 2013, a report published by Zheng explained the use of ZIF-67 as a sacrificial template for the synthesis of LDH nanocages, as supercapacitors, because of its excellent thermal and chemical stability and hardness. This was done to obtain the non-spherical LDH structures with controlled morphologies, as ZIF-67 is easily removeable in acidic solutions. The resulted structures exhibited better pseudo capacitance properties than the reported spherical LDH nanocages [34]. This gave the prospect of employing ZIF-67 as a sacrificial template for synthesizing intricate metal oxide structures with superior properties in their respective applications. Similarly, hollow Co_3O_4 were also synthesized by thermolysis of the ZIF-67 microcrystals, which showed better catalytic activity for CO oxidation [35].

Transition metal oxide has been most commonly used, with ceria being the exception, in collaboration with ZIF-67 to be used in various applications with a solid synergistic effect. Fischer et al [36, 37] were the first to show that MOFs could be used as hosts for transition metal oxides nanoclusters by gas-phase infiltration with organometallic precursors. Since then the advancements in this field have been at pace to study the distinct combinations in various research areas. ZIF-67 has been chosen as our MOF material, because of its excellent thermal and chemical stability, easy synthesis procedure, tailoring porosity, and tuneable morphology. There are extensive applications that covers this area of research, but our work focuses on the catalytic aspect of ZIF-67 in the field of heterogenous catalysis.

2.1.2 ZIF-67 as a catalyst

ZIF-67, itself, has been employed as a catalyst for a number of applications and in collaboration with transition metal cations and metal oxides, as well. In 2015, a report published by Lin, demonstrated the catalytic capability of ZIF-67 to activate peroxymonosulfate for the disintegration of RB in water. Previously, cobalt had been proved to be an efficient catalyst for PMS, therefore a cobalt-based MOF was preferential. It turned out to improve the degradation kinetics and magnitude considerably [38]. ZIF-67 has also been utilized as an effective catalyst for converting carbon dioxide to cyclic carbonates. It exhibited better activity and selectivity than previously reported ZIFs for the same reaction, as it required lower temperature and pressure, in addition to the higher conversion into the desired products [39].

Though ZIF-67 is still in its early stages of development as a functionalized industrial catalyst, its facile synthesis techniques and cost-effective nature, with better activity than most MOFs, makes it adequate enough to be functionalized at an industrial level. Other than being employed as a hetero-catalyst itself, ZIF-67 had also been doped with transition metals to produce structures with an enhanced synergistic impact. In 2012, Yang reported his work on Cu doping into ZIF-67, to fabricate a Cu/ZIF-67 photocatalyst. A higher adsorption capacity was observed for the doped structure. Since ZIF-67 has a porous structure, Cu^{+2} guest ions get affixed in these pores and results in better interaction with incoming gaseous molecules. Although, a complete structural mechanism for the resulted metal doped framework was still not explained in that report [40].

2.1.3 Cerium dioxide structures using ZIF-67

There are reports published on how ZIF-67 is employed for the synthesis of mixed metal oxides or hollow structures of cerium dioxide. In 2016, a report published by Zheng Peng Li described the synthesis procedure for hollow structures of cerium dioxide with a dodecahedral morphology, and its application as a heterogeneous catalyst for CO oxidation. In that research, ZIF-67 was utilized as a sacrificial template, that resulted in a morphologically perfect metal oxide catalyst, with an enhanced surface area [41]. Similarly, another report by Wang, in the same year, demonstrated the formation CeO_2-Co_3O_4 mixed catalyst obtained by the thermolysis of ZIF-67 at high temperatures. Wang

first pre-synthesized ceria nanowires and incorporated them into ZIF-67 porous structure. Further, this structure was thermally annealed to produce a mixed metal oxide catalyst with an enhanced catalytic activity [19]. The hollow structure of CeO_2 and embedded structure of CeO_2-Co_3O_4 mixed metal oxide, are shown in Fig. 3 and 4, respectively. In general, the synthesis of hybrid structures and specially ceria-based structures through conventional means is complicated because of the difficulties in incorporating materials, with definite chemical and physical properties, at the same time. Employing MOFs for their synthesis is a facile and a cost-effective choice to do that.

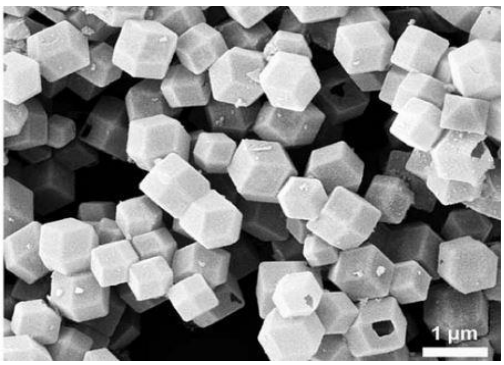

Figure 4 Hollow structure of ceria using ZIF-67 [19]

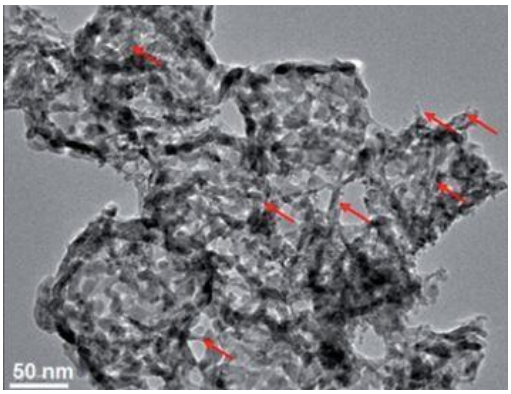

Figure 5 Ceria nanowires inserted Co_3O_4 mixed metal oxide [41]

2.2 Cerium dioxide in heterogenous catalysis

Cerium dioxide is one of the reducible oxides, that are characterized by their ability of exchanging oxygen, with the gaseous or a liquid phase surrounding them, through an easy way. This makes them an effective heterogenous catalyst. This is due to the availability of vacant cation d-orbitals in ceria, that do not have higher energy compared to the valence band. Expulsion of an oxygen atom from cerium dioxide results in surplus electrons that

are reallocated on the cation vacant regions, thus altering its oxidation state from +4 to +3 [4, 6]. On the other hand, non-reducible oxides such as SiO_2, MgO, etc., do not readily lose electrons or oxygen atom, because of the fundamental resistance of the associated metal cation to alter its oxidation state. The distinction between reducible and non-reducible oxides is significant for the chemical reactivity of these materials. Nowadays, a considerable number of industries deal with the oxidation or oxidizing dehydrogenation reactions. In majority reactions, the working catalyst is an oxide, and the reaction works on the mechanism initially represented by Mars and Van Krevelen (MvK). The basis of this mechanism states that the catalyst here actually takes part in the chemical reaction, through the active oxygen atoms it has, instead of just spectating it. This process can be descripted by the cost of withdrawing the oxygen atom from the surface of the catalyst. This, as a matter of fact, establishes both the kinetics and thermodynamics of the entire reaction. For that reason, the identification of generated oxygen vacancies on the catalytic oxide's surface is important and there are certain characterization equipment that are able to locate that. This would help in synthesizing oxide catalysts with required properties and improved reducibility. Doping of metal oxides with heteroatoms is one of the approaches that are used to produce metal oxide catalysts with enhanced reducibility and hence better catalytic activity [5].

2.2.1 Effect of Doping on Cerium Dioxide

Ceria has been doped with a number of metal ions with the purpose of promoting active oxygen atoms at the ceria's surface which eventually displays higher catalytic action. A few are discussed here that highlights the importance of metal doping into ceria's structure.

A report presented by Dan Yang, in 2010, discussed the doping of trivalent ion into CeO_2. Y^{+3} were used as the trivalent ion that could be doped into the cubic fluorite structure of CeO_2 through a hydrothermal process. It was suggested that increasing the dopant concentration to a certain ratio will result in an inhomogeneous crystal structure and the cubic fluorite structure of CeO_2 will be replaced by the cubic bixbyite structure of Y_2O_3 containing Ce^{+3} now the doping unit. Also, the oxygen vacancy defects in the doped ceria were proved to be concurrent with the concentration of the doping constituent, which in turn had a positive effect on the reducibility of the resulted product. Ceria doped with a

minor concentration of Y^{+3} resulted in an extremely distributive pattern of dopant cations that bonded with the oxygen vacancies uniformly, and thus increased the reducibility and catalytic capability of the material. Increasing the concentration of the dopant further resulted in the rearrangement of oxygen vacancies into regions where their motility was hindered and as a result, a reduced chemical reactivity was observed. So, the concentration of dopant to a definite ratio was concluded to be the key factor in determining the activity of the metal oxide catalysts [42].

Li et all, in 2011, suggested a two-step approach, through a hydrothermal process, for the formation of Ni doped CeO_2 necklace shaped nanowires, in an ethylene glycol and acidic medium. The role of ethylene glycol is to hinder the nucleating rate with its high viscosity, thus direct the state of surface nanocrystals and restrict their further development. This resulted into a highly directed growth of CeO_2 nanocrystals with ethylene glycol chains acting as stabilizing agents. Also, due to a lower rate of hydrolysis, ceria nanocrystals get attached to each other through interconnected glycol chains and ultimately transform into a larger aggregation by eliminating those glycol chains with the assistance of a strong acid. In that study, nitric acid was used as the acidic medium. The idea of development of ceria CeO_2 having a morphology of necklace nanowires brought the material a few particular highlights. Above all else, such polycrystalline structure displayed a smaller diameter and particle size with a relatively high surface area. Smaller grain size also gave rise to new surface defects [43].

2.2.2 Ceria doped with Cu

In 1998**,** Lj. Kundakovic talked about the catalytic activity of copper and silver modified CeO_2 catalysts for methane oxidation and also studied their reduction behavior using TPR technique. Cerium oxide was doped with La and Zr and then minute amounts of Cu and Ag were added to produce heterogenous metal and metal oxide catalysts. The research reported the improved reducible properties and action of ceria in redox responses presented by doping and by augmentation of transition metal or metal oxides. By incorporating a transition metal, a narrow crystalline size of CeO_2 favors the generation of exceedingly reducible oxygen species [44].

Knauth et al, in 1999, presented a ball milling technique for the synthesis of copper doped CeO_2. This was rather a complex technique but worked efficiently. The mixing of CeO_2

with fitting quantities of Cu_2O took place before the milling, emphasizing the importance of a certain concentration of Cu_2O that would be completely dissolved in a CeO_2 cubic fluorite structure. $Cu_{0.15}Ce_{0.85}O_{2-x}$ was prepared and samples having x greater than 0.15 exhibited XRD peaks of pure Cu_2O in spite of the ball milling, indicating the limit of solubility of Copper oxide in nanocrystalline CeO_2 [45].

In 1999, Daniela Terribile published her work on the oxidation of methane and other hydrocarbons by synthesizing Cu doped CeO_2. With the copper doped ceria sample, the initial intake of hydrogen occurred at 105 ˚C with the maximal at 210 ˚C. The quantity of hydrogen that was absorbed exceeded the amount prerequisite for CuO present in the sample. This was because a considerable extent of Ce^{4+} was reduced as well at these much lower temperatures. Other than that, H_2 species also integrates into the lattice which increases the total quantity of hydrogen consumed, and thus increases the chances of reduction of primary cation at much lower temperatures. Daniella concluded that the better activity of the doped CeO_2 catalysts corresponds to the insertion of defect sites which is due to the expanded oxygen movability [46].

In the same year, Andreas Tschope behavior of Cu-doped CeO_2 through reported his study on the oxidation-reduction the characterization techniques of XPS and Isothermal gravimetric analysis. The XRD results suggested that the samples annealed above 500 ˚C exhibited small peaks of CuO phase, which proved the presumption of Cu^{2+} being less soluble in the CeO_2 crystal lattice. Also, a metastability for segregated Cu ions was suggested on the surface of cerium oxide nanostructure. Cu ions highly scattered on the surface of ceria nanocrystals are more promising, with respect to thermodynamics, as compared to an additional precipitated phase, given that the particular surface zone of the CeO_2 lattice is sufficient enough to guarantee sub monolayer inclusion. Results derived from XPS and IGA exhibited that the uniformly distributed Cu ions on the ceria surface were prompt to reduce and oxidize at temperatures of about 200 ˚C. Also, the valence states of Cu were discovered to be +1, +2, and 0 dependent on their reduced and oxidized states [47].

Yue Li et al, in 2000, studied the behavior of copper and nickel doped ceria catalysts over water gas shift reaction. Kinetic study of the above-mentioned WGS reaction displayed relatively better results for 5 % of copper inserted into the ceria lattice as the activation

energy for these catalysts were much lower, even lower than some of the commercially available Cu with ZnO catalysts. At that time, under a WGS reaction the definite condition of Cu on the ceria surface was still ambiguous. Ceria doped with Cu showed remarkably enhanced activity than Ni doped ceria for a WGS reaction. In conclusion, it was said that the Cu-ceria catalyst entails almost no activation energy and maintains greater WGS activity at temperatures as high as 600 ˚C [48].

Later in 2005, a study was conducted on the electronic and structural properties of Cerium dioxide doped with different concentrations of Cu ion. This gave a little detailed insight into the structural behavior of the Cu doped catalysts which had not been done before. Comparison of the ionic sizes, lattice parameters, O atom bonds, generated oxygen vacancies, the redox behavior between pure metal oxides of cerium and copper with copper doped structures were presented. It was concluded that the Cu atom inserted into ceria lattice exhibited an oxidation state greater than its oxidation state of its respective oxides of Cu_2O and CuO. One of the other structural results showed a bit strange or a deformed structure of the resulted doped metal oxide which is attributed to local order defects and multiplex cation to oxygen bond lengths as compared to bond lengths appeared in a pure ceria crystal. This obviously brought upon the generation of more oxygen vacancies. The reduction of $Ce_{1-x}Cu_xO_2$ was totally reversible not showing any substantial sign of formation of Cu_2O or CuO in the process of further oxidation [49].

Yang et al published his work, in 2014, on the synthesis and characterization of copper doped ceria nanospheres and their catalytic activity for CO oxidation. The synthesis involved a one-step hydrothermal process which resulted a decrease in the size of Cu^{+2} doped ceria nanospheres in comparison to pure ceria, prepared by means of the same method. The Copper ions were proved to have a vital part in the growth of ceria nanospheres. It was also presented that the morphology and diameter of the resulted nanospheres is not affected by the different amounts of copper ions added into the solution. Ceria is believed to have a better oxidation capability because of its +3 and +4 oxidation states, which is further increased by the addition of Cu^{+2} due to the valency variance among Cu^{+2} and Ce^{+4}. Moreover, the Cu^{+2} doped samples were proved to have a higher surface area due to their rugged surface and the induction of more oxygen voids give rise to certain crystallography defects in the resulted samples, as compared to pure

ceria. The reducibility of the metal doped catalyst is also affected by the amount of copper ions added which give rise to two reduction peaks at lower temperatures than for pure ceria, for their H_2-TPR profiles. This can be credited to the reduction of copper units on the exterior at lower temperature and interior copper ions at a higher temperature which behave as substitutive defects in the space lattice of ceria. The catalytic capability of the prepared copper doped samples was further investigated by a CO oxidation reaction in which the copper doped ceria, with a ratio of 0.10, exhibited a much higher performance at lower temperature as compared to ceria microspheres and commercial CeO_2 powders. This was because of the higher surface area of the resulted product and also copper ions tend to create more oxygen vacant sites when they are integrated into CeO_2 nanospheres and hence better reducibility [50].

CHAPTER 3

Materials and Methods

Our work is based on the synthesis of ceria nanoparticles and their transition metal doped structure as well as ceria nanoparticles embedded inside MOFs. The MOF chosen here is ZIF-67. Following is a step by step description of synthesis process of each sample.

3.1 Synthesis of CeO_2 nanoparticles

Ceria nanoparticles are prepared by a hydrothermal method which is in accordance with the work proposed by Ming Lin [51].

3.1.1 Materials used

Cerium nitrate hexahydrate, M= 434.23 g/mol, was purchased from MERCK KGaA. Polyvinyl pyrrolidone and sodium hydroxide were also purchased from MERCK KGaA. For centrifugation and washing, absolute ethanol was used (LAB SCAN Analytical Sciences). Deionized water was used as a solvent.

3.1.2 Experimental details

Firstly, 0.9 g of PVP is dissolved in 30 ml of deionized water. This solution is stirred for a while under magnetic stirring. After sometime, 1mmol of Ce $(NO_3)_3.6H_2O$ i.e. 0.434 g, is dissolved in that mixture. Next, 1 mmol of NaOH i.e.0.04 g, is taken and dissolved in the mixture. This mixture is stirred for 30 min under magnetic stirring, at room temperature. The solution is then transferred to a 50 ml Teflon lined autoclave. The autoclave was put into a heating oven. It was kept inside the oven for 24 h at 180 ˚C. After that, the autoclave was taken out of the oven and left to cool down. Precipitates were collected after centrifugation of the synthesized solution. It was done for 30 min at 4500 rpm. These were also washed thrice with ethanol and DI water. At last, the obtained particles were dried in an air oven at 80 ˚C for 2 h.

3.2 Synthesis of ZIF-67

ZIF-67 polyhedrons are synthesized by a facile technique that involves the mixing of materials as well as the formation of polyhedrons, all at room temperature. This method is in accordance with the report published by Zheng Jiang [34].

3.2.1 Materials used

2-Methylimidazole, M= 82.11 g/mol, was purchased from MERCK KGaA. Cobalt Nitrate 6-hydrtae, M= 291.07 g/mol, was purchased from UNI-CHEM Chemical Reagents. Absolute methanol was used as a solvent. For washing, absolute ethanol was utilized.

3.2.1 Experimental detail

First of all, 0.291 g (1mmol) of Cobalt nitrate is dissolved in 25 ml of methanol. Another solution was prepared by mixing 0.328 g of 2-methylimidazole in 25 ml of methanol. These two solutions were then mixed under room temperature. The cobalt nitrate solution (red in color) is added to the methylimidazole solution (transparent). A purple color solution was obtained after mixing the two solutions. This was stirred for almost 5 to 10 min under magnetic stirring. The mixture was aged for 3 days at room temperature. Precipitates were collected by centrifugation for 30 min at 4500 rpm, at room temperature, and washed with ethanol thrice. Purple color precipitates of ZIF-67 were obtained after being dried at room temperature.

3.3 Synthesis of ZIF-67/CeO_2

3.3.1 Materials used

2-Methylimidazole, M= 82.11 g/mol, was purchased from MERCK KGaA. Cobalt Nitrate 6-hydrtae, M= 291.07 g/mol, was purchased from UNI-CHEM Chemical Reagents. Absolute methanol was used as a solvent. For washing, absolute ethanol was employed.

3.3.1 Experimental Details

Typically, 20 mg of the as-prepared ceria nanoparticles were dispersed in 20 ml of absolute methanol, under ultrasonication at room temperature. After sometime, 0.328 g of 2-methylimidazole powder is added in that solution under vigorous stirring. This was stirred for another 30 min. Let that solution be solution one. Next, another solution of

cobalt nitrate in methanol was prepared at room temperature. 0.291 g of cobalt nitrate was dissolved in 5 ml of absolute methanol to obtain a red colored solution. This red colored solution was dissolved in solution one, and stirred for a while. The obtained solution was aged for 3 days at room temperature. This was followed by centrifugation for 30 min at 4500 rpm, to obtain the purple colored precipitates. These were washed with ethanol three times and dried at room temperature to get the final product.

3.4 Synthesis of Cu doped CeO_2

Copper doped Ceria sample was prepared by a hydrothermal method and in accordance with the report published by Yang [50].

3.4.1 Materials used

Cerium nitrate Hexahydrate, M= 434.23 g/mol, was purchased from MERCK KGaA. Copper nitrate 3-hydrate, M= 241.60 g/mol, was purchased from Riedel-de Haen. Polyvinyl pyrrolidone, sodium hydroxide, and hydrogen peroxide were purchased from MERCK KGaA. Deionized water was used as a solvent. Absolute ethanol was used for washing.

3.4.2 Experimental details

First of all, 1.17 g of ($Ce(NO_3)_3 \cdot 6H_2O$) and 0.2 g of PVP were dissolved in 19 ml of DI water. PVP was dissolved first. This solution was stirred for a while until PVP is completely dissolved. It was followed by the addition of 0.9 ml of $Cu(NO_3)_2 \cdot 3H_2O$ (5 g L^{-1}) and 0.1 ml of H_2O_2, under vigorous stirring for 30 min. A transparent solution was obtained. This solution was then transferred to a 50 ml Teflon lined autoclave and heated for 5 h at 180 ˚C. The resulted precipitates were collected by centrifugation for 30 min at 4500 rpm, at room temperature, followed by washing with ethanol three times. Finally, the dried product was obtained by heating it in an oven for 6 h at 70 ˚C. The obtained powder is yellow in color.

CHAPTER 4

Characterization Techniques

4.1 X-ray Diffraction

XRD is an analytical technique which is used to identify the crystal structure, calculate the lattice parameters, measure stresses in materials, and crystallographic texture. The basic purpose of this is to identify the phase of materials like powders, thin films, or membranes. It could be polycrystalline or amorphous. It works on the principle of constructive diffraction. In case of crystalline materials, beautiful diffraction patterns of the samples are obtained, even if it is a small crystal. But if it is an amorphous material, very little diffraction pattern is obtained, because of the presence of short-range orders in amorphous materials and lack of a perfect crystal lattice. Hence, we do not get the strongly reinforced diffraction grating like pattern [52].

4.1.1 Working Principle

XRD works on a principle of Braggs Equation which was invented by an English physicist Max Von Laue, in 1912. X-rays have very high energy like other electromagnetic rays with wavelengths in the range of 0.1 to 100 Å. Fig. 5 shows a crystal plane and X-rays incident on them. If we have light coming in here to the crystal, some of it will reflect off and more of it will continue to reflect on and might reflect off on another point. And therefore, these two points would have different path lengths and they would form a perfect diffraction pattern. The approximate distance between the planes is 1 Å. X-rays have wavelengths comparable to that and therefore they are allowed to pass through different crystal lattice and that way information about the structure of materials can be obtained through their diffraction patterns. The Braggs law is defined by the following equation,

$$m\lambda=2d\sin\theta \quad (1)$$

Here, m=1,2, 3, …

λ= wavelength of the x-ray,

d= distance between two atoms

θ= the angle which the incident wave makes with the crystal lattice plane

This law says that the two x-rays will interfere constructively only if they travel a distance that is equal to a whole number multiple of their wavelengths, i.e., when the two waves are fully in phase. If the wavelength is known, θ could be measured, and then d could be found out between the two atoms [52].

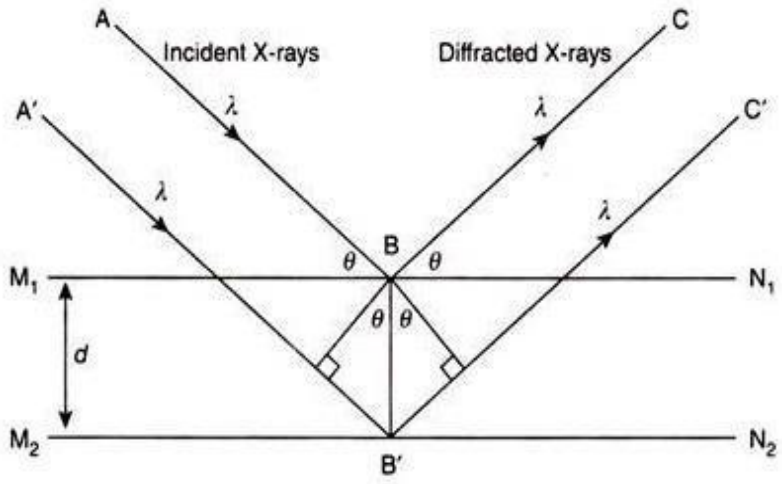

Figure 6 Working principle of XRD [52]

4.2 SEM/TEM

SEM is an abbreviation for Scanning electron microscope. It is used to analyze the morphology, particle size, and shape of the materials. It uses electrons for imaging, in the same way as light microscope employs visible light. Fig. 6 shows a schematic of the SEM equipment. Electrons are generated at the upper part of the column, that accelerates down and go through a set of lenses and apertures to create a concentrated beam of electrons, which strike the surface of the material. The sample is fixed on a stage in the chamber region, and unless the microscope is made to function at low vacuum, both the chamber

and the column are vacated by a set of pumps. The degree of vacuum depends on the designed conditions of the microscope [53].

4.2.1 Working Principle of SEM

Electrons, upon interacting with the sample, generate secondary electrons, backscattering electrons, and X-rays. These are assembled one or several detectors to create images, which are then showed on a computer screen. When the electrons strike the surface of the sample, it permeates through the sample to a distance of small number of microns. This depends on the accelerated voltage and denseness of the material. Signals, like secondary electrons and X-rays, are generated as an outcome of this contact with the interior of the material [53].

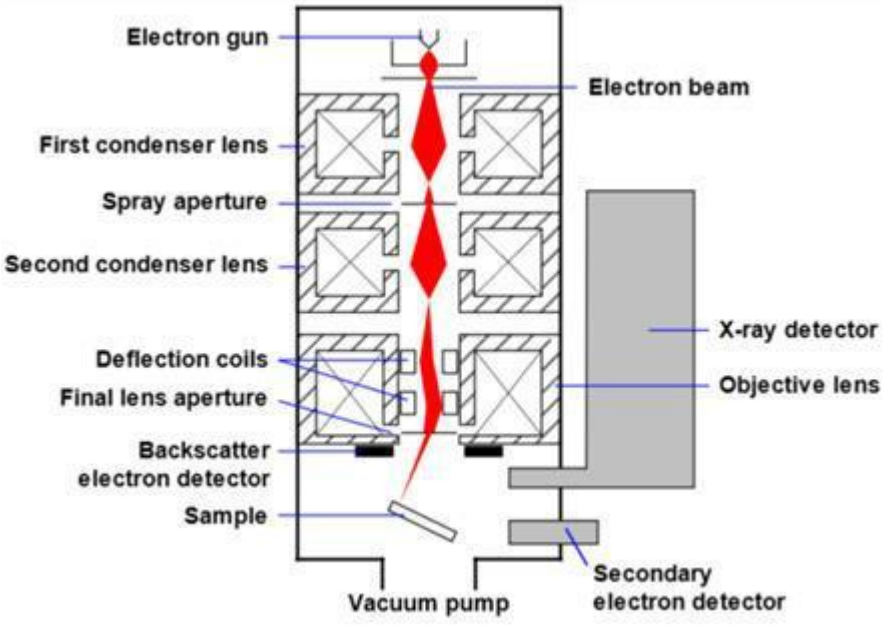

Figure 7 Schematic of Scanning Electron Microscope [53]

4.2.2 TEM

TEM stands for Transmission Electron Microscopy. In this technique, a beam of electrons is made to pass through the sample, which is a very thin segment, on a grid. Then the images are produced as a result of the contact between the electrons and the material. The obtained images are centered on a photographic device such as a fluorescent screen. It is different from SEM in a way that it uses transmitted electrons to form an image. This way

it provides information about the internal structure of the sample, like the crystal structure, morphology, and stress positions, while SEM produce results about the surface of the material and its composition. The other difference lies in the optimum resolution that they can attain; SEM resolution is restricted to ~0.5nm, whereas with latest advances in TEAM (Transmission Electron Aberration Corrected Microscope), images with special resolution of much less than 50pm are published [54].

4.3 EDS

Energy Dispersive X-ray is an analytical technique used for identification of materials and the presence of contaminants, as well as determining the elemental compositions of materials. EDX analysis provides qualitative and quantitative atomic data related to materials. Elemental composition information is shown by intensity of lines related to each element is provided by quantitative analysis. While for qualitative analysis, identification is done simply by X-ray spectrum [55].

4.3.1 Working Principle of EDS

The working principle is based on electromagnetic radiation interaction with matter, which results in a collision with inner shell electron and ejects it from the atom causing a gap in an inner layer. The gap is filled by the electron from the outer shell. This results in energy loss which causes an emission of X-rays from matter when being targeted by charged particles. Each element generates its own characteristic X-rays which contains information about it. Later, after atom ionization two key events occur in the form of elastic scattering and an inelastic scattering. The elastic scattering is direction adjustment of the electron with no prominent loss of energy which is because of an interaction of the beam of electrons with nucleus while inelastic scattering is quite opposite of it. Photon energy sensitive detector is used for determining emission of X-rays at a different wavelength related to the particular element. EDX analyze two different kinds of radiations; continuous radiation which provides a foundation for measurement and characteristic radiation [55]. The working principle is also shown in Fig. 8.

Mostly EDX is used for detection of high atomic number elements. Light elements having an atomic number less than 11 are difficult to be analyzed by EDX. EDS technique

determines a distribution of each and every element as well as their morphological properties [55].

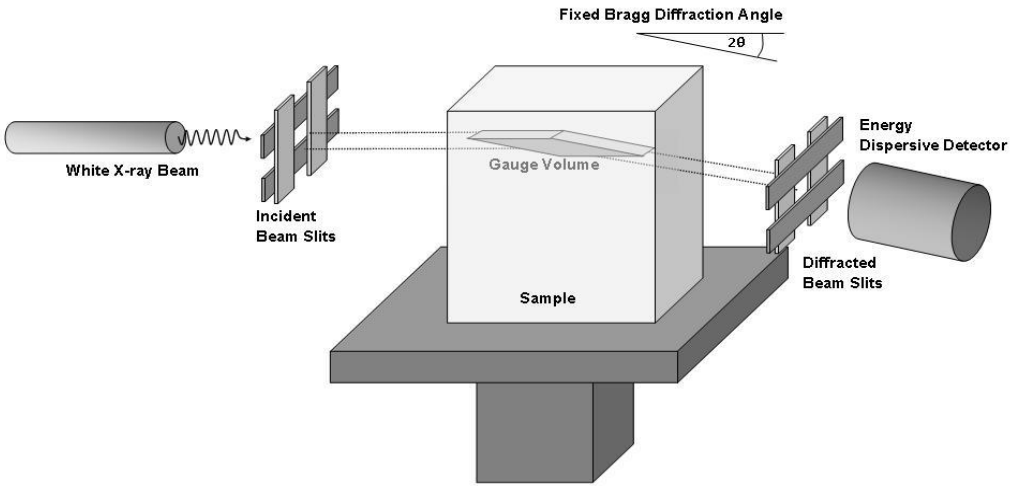

Figure 8 Working principle of Energy-dispersive X-ray spectroscopy [55]

4.4 FTIR

FTIR stands for Fourier Transform Infrared spectroscopy. It is a kind of techniques which produce an infrared spectrum of absorption or emission of a solid, liquid, or a gas. It generates the data based on the vibrations of functional groups that lie in the material, and hence the variety of chemical bonds present in a sample can be easily identified. Its energy range generally lies from 400 to 4000 cm^{-1} [56].

4.4.1 Working Principle

FTIR works on the principle of interaction of matter with light. In this case, the electromagnetic radiation strikes the surface of the material, and an infrared spectrum of that material is obtained, only if the sample contains a constant or induced dipole moment and the energized vibrational states. There is an interferometer present in the equipment, that guides the IR radiation and calculate all of the IR frequencies. After being passed through the sample, obtained signal is interferogram. The data is then acquired and altered from an interference pattern into a spectrum. through Fourier transformation. The spectra produced, are usually displayed as a plot between intensity and the wavenumber (cm^{-1}). It is very simple to use with very little quantity of samples required, and the characterization time is generally less than five minutes. It is excellent for the qualitative

study of the sample but a little less adequate when analyzing the sample quantitatively [56, 57]. Fig. 9 shows the schematic of the FTIR spectrometer.

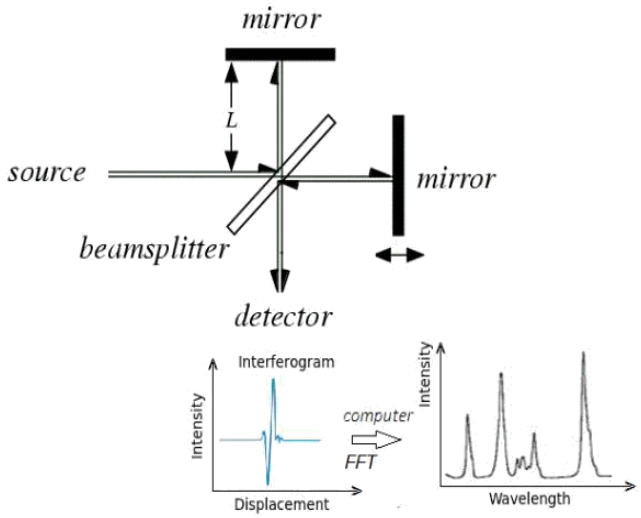

Figure 9 Sketch of FTIR Spectrometer [56]

4.5 TG/DTA

TG/DTA stands for Thermogravimetric/Differential Thermal Analyzer and it is used to analyze the thermal stability of the proposed sample. It mostly gives information about the physical processes occurring in a material. It measures the material's masses with time, as the temperature is continually being changed or sometimes at a fixed temperature. It is employed to study the decomposition and evaporation rates of a sample, oxidation, and presence of any impurity could also be detected [58].

4.5.1 Working Principle

It is performed in an environment expurgated with a gas and also in vacuum. Usually the gases employed are nitrogen or air. The equipment comprises of a precision balance along with a pan that carries the sample, placed in a furnace that also contains a programmable controlled temperature. The temperature usually increases at a fixed rate to induce a thermic reaction. This reaction might take place in different atmospheres, such as, air, nitrogen or any other inert gas, vacuum, or a self-induced atmosphere, in addition to various pressures, like high pressure, regulated pressure, fixed pressure, or high vacuum. The results obtained are in a form of a plot of mass percentage or weight loss percentage

on the y-axis while the temperature is on x-axis. Also, DTA curve, which is the first derivative of TGA, is also obtained for a detailed insight. It tells us about the point or temperature at which heat is absorbed or released during a chemical reaction, and thus its endothermic or exothermic nature. The temperature generally reaches a 1000 degree Celsius. Materials, which can be analyzed using this thermal analyzer include all kinds of metals, polymers, even ceramics or glass [58]. Fig. 10 shows the block diagram of a TG/DTA equipment.

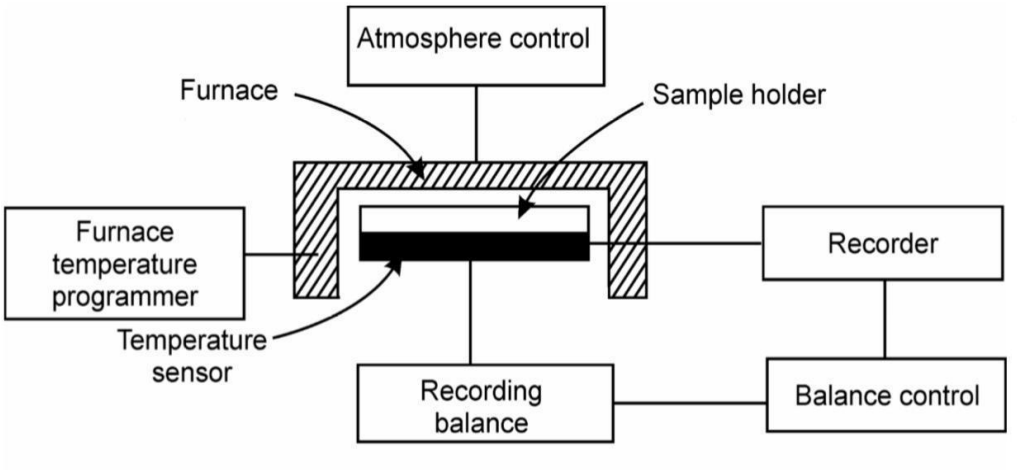

Figure 10 Block diagram of TG/DTA [58]

4.6 TPR

It stands for Temperature Programmed Reduction. As the name implies, this technique is employed to study the sample's reductive behavior under a programmed temperature environment. It is the best technique available for analyzing the catalyst's behavior or activity. It is also used to study the heterogenous aspect of the materials. These include metal oxides, or mixture of metal oxides, or any supported metal oxide. The TPR profiles provides information about the qualitative nature of the catalysts, in terms of their maximum reduction temperature, effect of the chemical changes occurring from the supports attached (if any) [59].

4.6.1 Working Principle

This technique involves the overflow of a gaseous mixture (usually 3 to 17 % of hydrogen gas mixed with inert gases like argon or nitrogen) past the sample. The sample will absorb

the gaseous mixture according to its own capacity of absorbance or its reductive behavior, at a specific temperature. This is specific for every material. The exiting gas streams will have a different composition and that is measured by a thermal conductivity conductor (TCD). The detector's result is then transformed into concentration of the active gas through level calibration. The final graphs are obtained in the form of amount of gas absorbed vs temperature. The equipment consists of a plain and simple U-type container which carries the catalyst. That U-type container is located inside the furnace, and also attached with a thermocouple. Flow controllers are also affixed to regulate the flow of the reducing gas mixture. Water is produced as a by-product in this reaction. Measuring the amount of water produced is a more accurate way of measuring the reduction. This is because of the possibility of altering hydrogen's concentration at the inlet, so any change in this concentration will result in a different amount of water produced, as the initial concentration of water is zero [59]. Fig. 11 shows the schematic of TPR equipment.

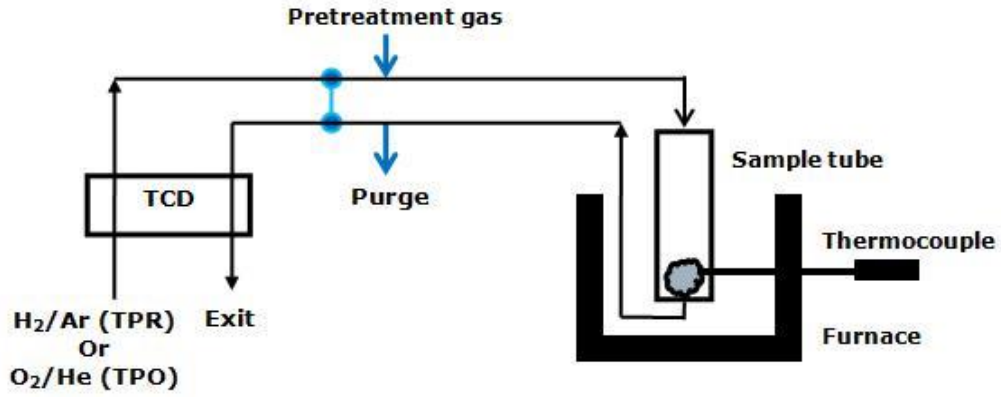

Figure 11 Schematic of Temperature Programmed Reduction equipment [11]

4.6 XPS

XPS is an abbreviation for X-rays photoelectron spectroscopy. It is a surface analysis technique that is used to study the chemical composition of various materials, structure of atoms or electronic structure of elements, as well as ionization energies. It also informs us about the chemical nature of bonds present between these elements. It is a non-destructive technique, though it is very expensive and requires longer processing time with high vacuum [60].

4.7.1 Working Principle

It works on the principle of photoelectric effect which was invented by Albert Einstein in 1905. It involves irradiating the sample with an x-ray beam and then quantifying the kinetic energies and the number of electrons that are ejected from the material. X-rays have their own energy with a particular wavelength that is known. These X-rays are absorbed by the material and then inner shell electrons are ejected with particular kinetic energies that can be calculated. It is shown by the following equation,

$$E_{binding} = E_{photon} - (E_{kinetic} + \boldsymbol{\phi}) \quad (2)$$

Here $E_{binding}$ is the binding energy of the electrons, E_{photon} is the energy of the x-ray which is known, $E_{kinetic}$ is the kinetic energy of the ejected electrons that can be measured, and ϕ is the work function that depends on both the sample and the spectrometer. The above equation shows the conservation of energy based on the work of Ernest Rutherford in 1914. The equipment consists of an electron energy analyzer, an x-ray source, vacuum system, and computer system. The resulted XPS spectrum is the plot of binding energies of the ejected electrons versus the intensity of these peaks. The binding energies of the electrons are specific for each material and this is how they get identified [60]. Fig. 12 shows the schematic diagram of an XPS equipment.

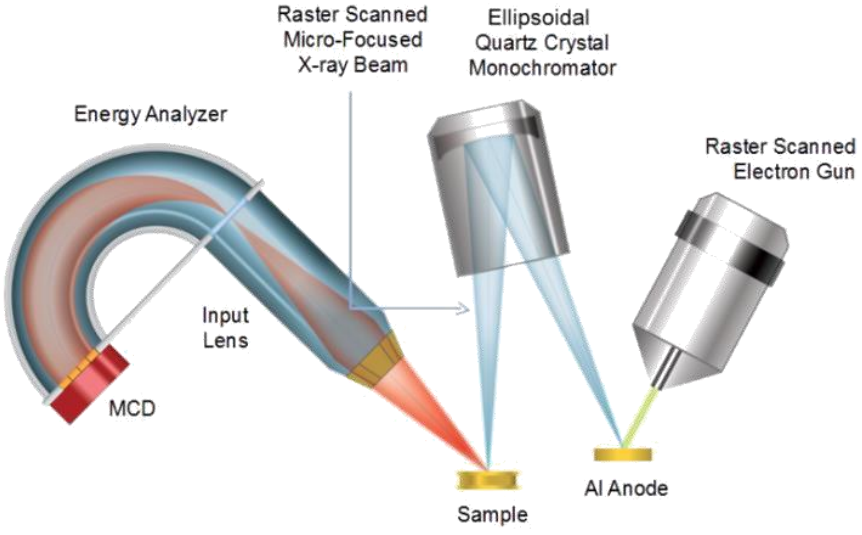

Figure 12 Schematic diagram of X-ray Photoelectron Spectroscopy [60]

Chapter 5

Results and Discussion

5.1 XRD Results

XRD pattern of as prepared ZIF-67 polyhedrons is shown in Fig. 13.

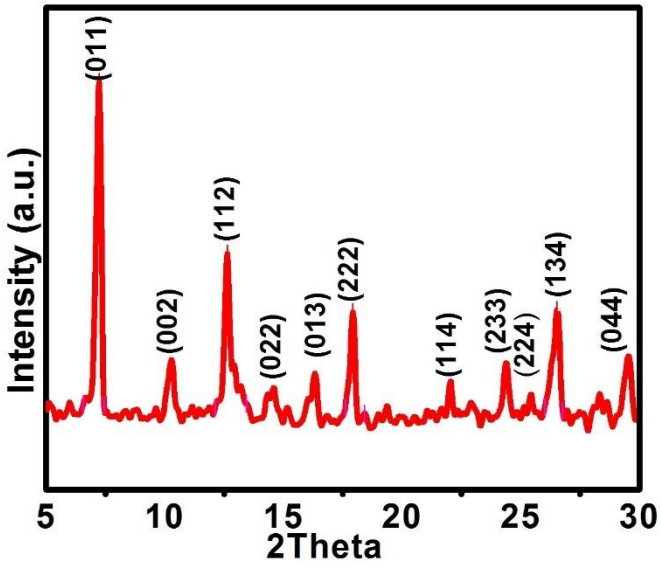

Figure 13 XRD pattern of ZIF-67 sample

The obtained XRD pattern illustrates the formation of well-crystalline ZIF-67 polyhedrons and are pure phase. The sharp and narrow peaks in the XRD pattern demonstrate the high crystallinity of ZIF-67 polyhedral structures. The particle size of ZIF-67 was calculated to be 113 nm by the following Debye-Scherrer equation

$$T = \frac{K\lambda}{\beta \cos\theta} \qquad (3)$$

Where, T is the mean particle size

K is a dimensionless factor

λ is the x-ray wavelength

β is the line broadening at half the maximum intensity (FWHM)

θ is the Bragg angle

Fig. 14 shows the XRD pattern of CeO_2 nanoparticles prepared through a hydrothermal method, with the Ce^{+3}/OH^- ratio of 1:1. The obtained diffraction peaks can be ascribed to the face-centered cubic fluorite structure of CeO_2 (a = 0.5411 nm).

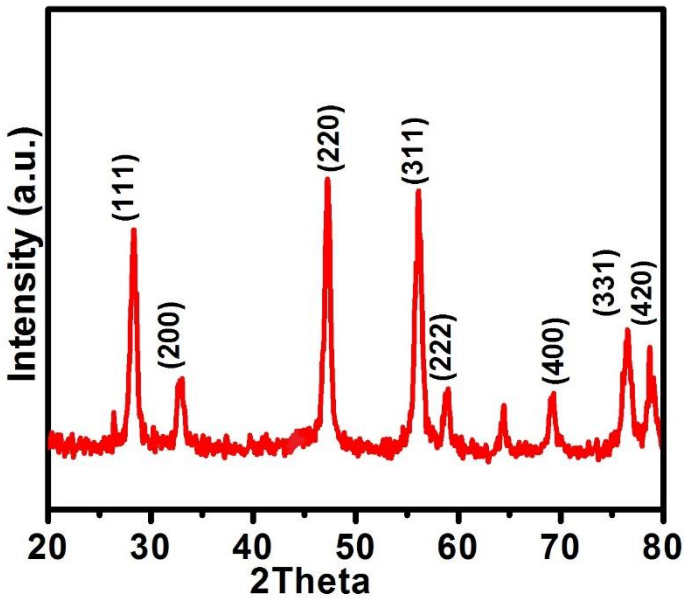

Figure 14 XRD pattern of pure CeO_2

The higher intensity peaks were obtained at 28.53, 47.5, and 56.26, corresponding to the crystal planes of 111, 220, and 311, respectively. From the literature, it is studied that the size and crystallinity of ceria nanoparticles changes with using different ratios of Ce^{+3}/OH. Herein, we have used 1:1 ratio of Ce^{+3}/OH^- to obtain well-dispersed crystalline ceria nanoparticles [51]. Its crystal size was found to be 26 nm. Fig. 15 shows the XRD pattern of ZIF-67/CeO_2 nanoparticles. Ceria nanoparticles were pre-dispersed, under ultrasonication, into ZIF-67 polyhedrons at room temperature. Herein, we can clearly see the diffraction peaks of both ZIF-67 and CeO_2. The diffraction peaks of ceria, that is encapsulated into polyhedral ZIF-67, is equally visible to ZIF-67 because of its well crystalline nature. The diffraction peaks from 5 up to 28˚ are ascribed to the presence of ZIF-67, while further peaks from 30 to 80˚ confirm the presence of ceria nanoparticles in the prepared sample. Its particle size was calculated to be 118 nm.

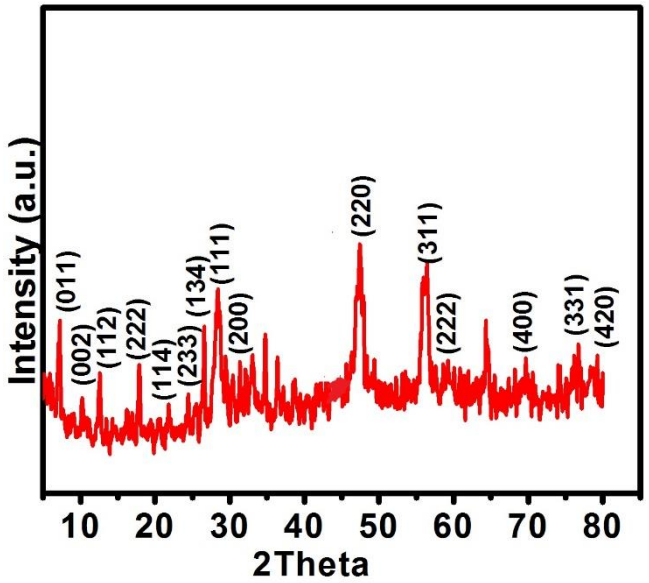

Figure 15 XRD pattern of ZIF-67/CeO_2

Fig. 16 shows the XRD pattern of Cu doped CeO_2. It was prepared through a hydrothermal method with 10% molar ratio of Cu^{+2} [50]. All the diffraction peaks displayed in the pattern correspond to the FCC fluorite structure of Ceria, with no sign of CuO, or Cu_2O, or $CeOHCO_3$, which demonstrates the uniformity and purity of the doped sample. The narrow and strong peaks confirm the formation of a well crystalline Cu doped structure. Its particle size was calculated to be 21 nm.

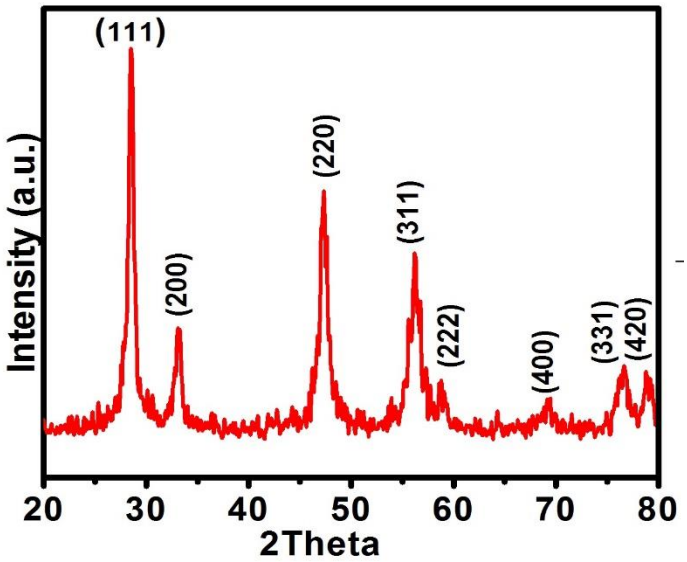

Figure 16 XRD Pattern of Cu doped CeO_2

5.2 SEM/TEM Images

Fig. 17 shows the SEM images obtained for as-prepared ZIF-67 polyhedrons and ceria nanoparticles.

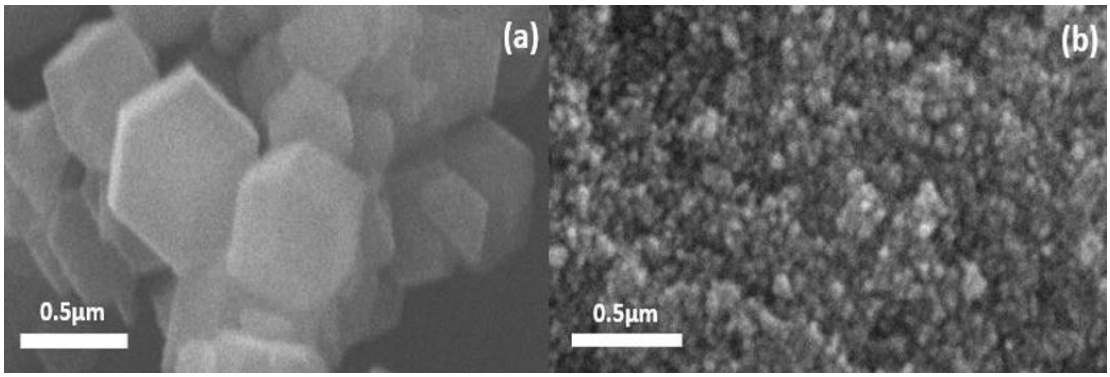

Figure 17 SEM images of (a) ZIF-67, (b) Pure CeO_2

Part (a) shows the dodecahedral morphology of ZIF-67. The size of the ZIF-67 crystals range from 600-800 nm. According to literature, methyl imidazole should always be used in excess to cobalt nitrate. This is because methyl imidazole does not act only as an organic linker during the synthesis, but also as a stabilizing agent in its neutral form, which is advantageous for fabricating uniform dodecahedral ZIF-67 crystals [35]. Part (b) shows the morphology of CeO_2 nanoparticles prepared through a hydrothermal method. The obtained nanoparticles display almost spherical morphology with uniform size ranging from 20-30 nm. The shape and size of ceria nanoparticle is reported to increase with increasing molar ratio of the alkali used [51]. Herein, a 1:1 ratio of the reactants was used to fabricate these. Fig. 18 demonstrates the dodecahedral morphology of ZIF-67/CeO_2 nanoparticles. Herein, we can see the small ceria nanoparticles being mounted on the surface of ZIF-67 polyhedrons. However, it is not possible to see the embedded ceria particles into ZIF-67 structure, therefore TEM images of this sample are also shown in Fig. 19. These range in size from 600-700 nm and are uniformly distributed.

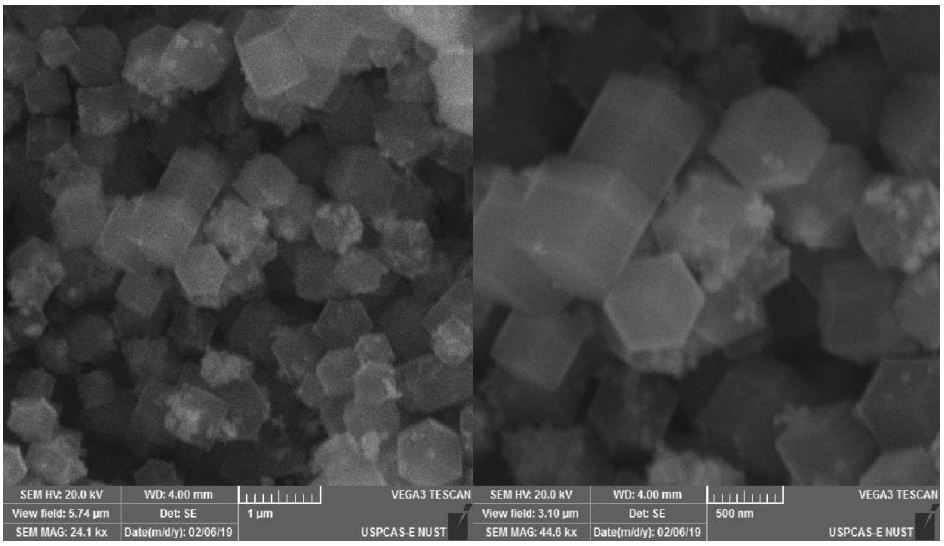

Figure 18 SEM images of ZIF-67/CeO_2

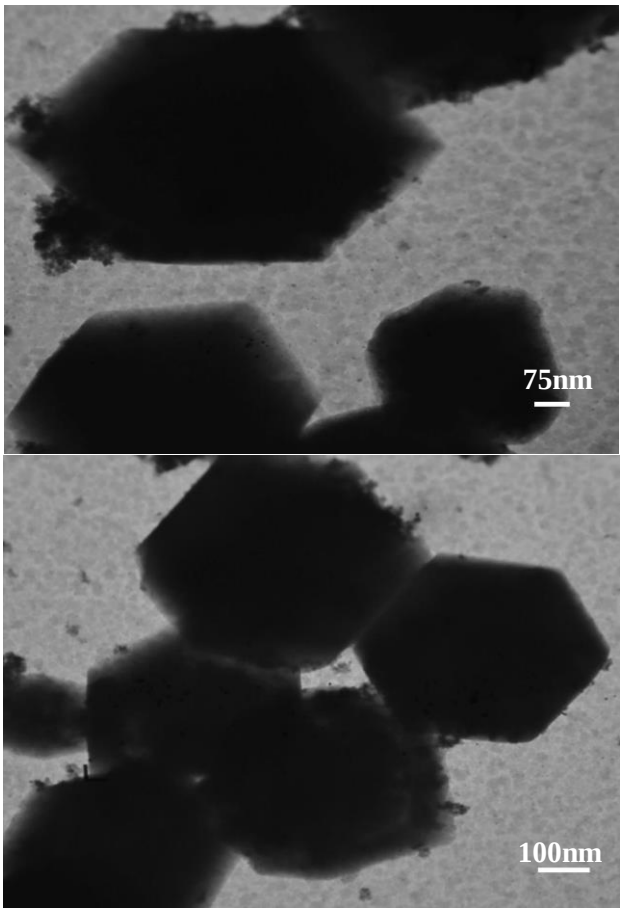

Figure 19 TEM images of ZIF-67/CeO_2

TEM images in Fig. 19 display the dodecahedral morphology of ZIF-67 particles measuring 750-900 nm in size. Another tiny range of particles having low interference with electron beam are also detected, these are attached / mounted on to surface of larger particles and also partly embedded inside the polyhedrons. These are ceria nanoparticles and were measured 30-40 nm in size. Fig. 20 shows the Cu doped Ceria nanospheres ranging in diameter from 40-50nm. From the literature, pure ceria nanospheres prepared under the same conditions have diameters much larger than that [50]. It demonstrates the function of Cu in the growth process of ceria nanospheres.

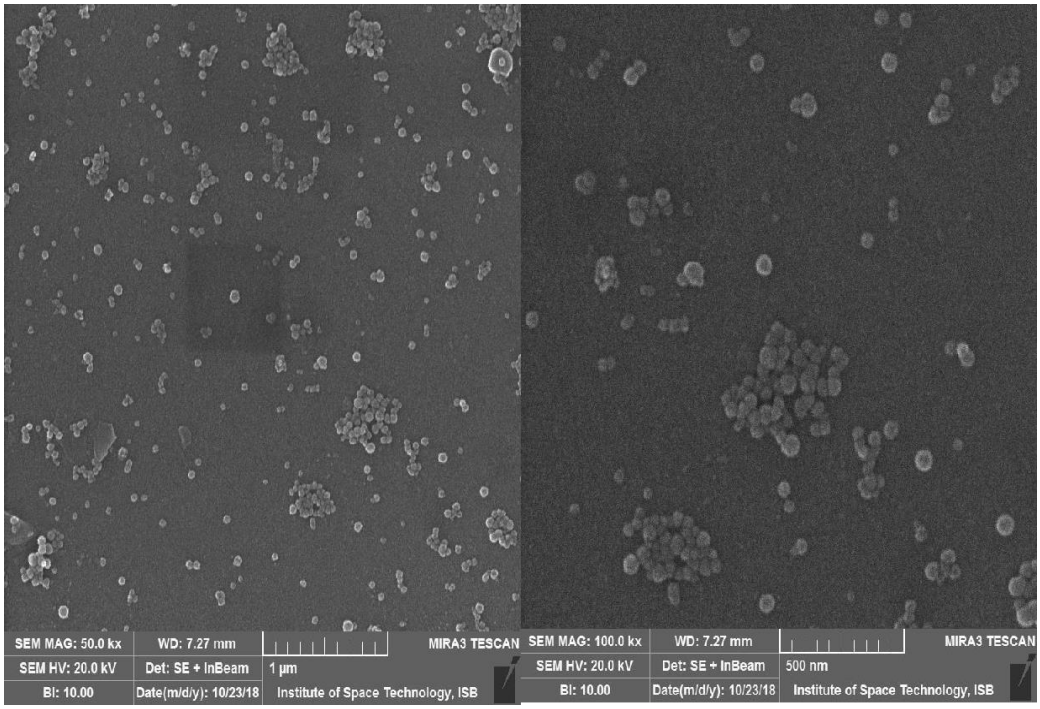

Figure 20 SEM images of Cu doped Ceria

5.3 EDS Spectrum

Energy dispersive spectroscopy analysis was performed on our samples to confirm the presence of desired particles. Fig. 21 shows the EDS spectrum of ZIF-67/CeO_2 with the percentage concentration of elements in Table 1. It was demonstrated that the particles in the sample were consisted of the elements Co, Ce, O, N, and C, supporting the presence of Ce along with Co, O, and N.

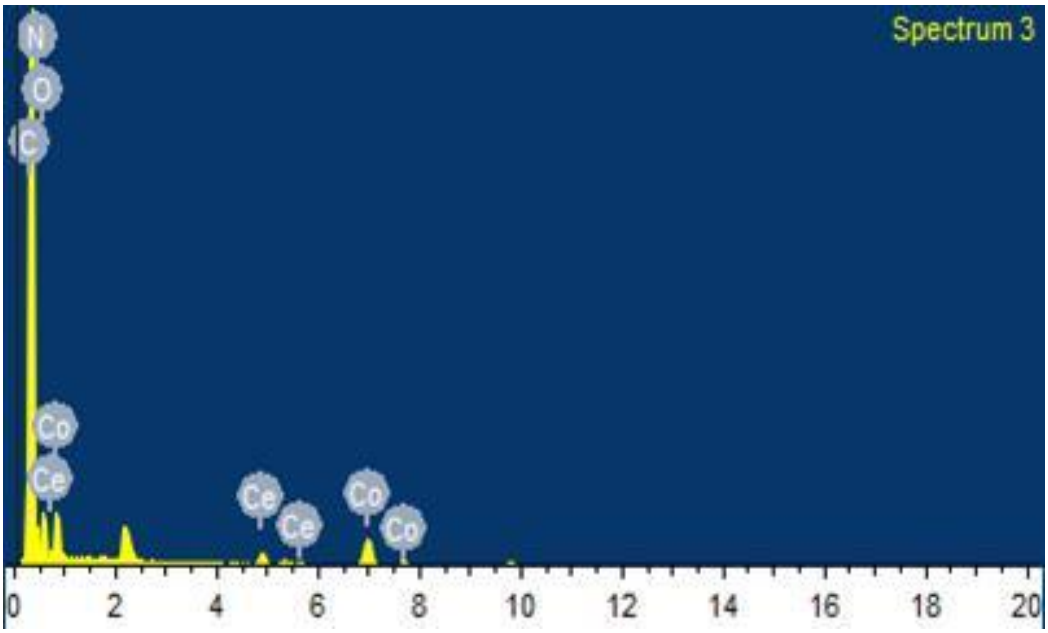

Figure 21 EDS spectrum of ZIF-67/CeO_2

Table 1 Elemental analysis of ZIF-67/CeO_2

Element	App Conc.	Intensity Corrn.	Weight%	Weight% Sigma	Atomic%
C K	128.63	0.5993	58.39	1.66	65.14
N K	3.42	0.0429	21.66	2.11	20.72
O K	10.25	0.1742	16.01	0.80	13.41
Co K	7.40	0.7490	2.69	0.12	0.61
Ce L	3.44	0.7508	1.25	0.10	0.12
Totals			100.00		

EDS spectrum of the Cu doped ceria sample is shown in Fig. 22. It demonstrates the presence of Cu along with Ce and O confirming the formation of a doped sample. The percentage element concentration is shown in Table 2 for the Cu doped Ceria sample.

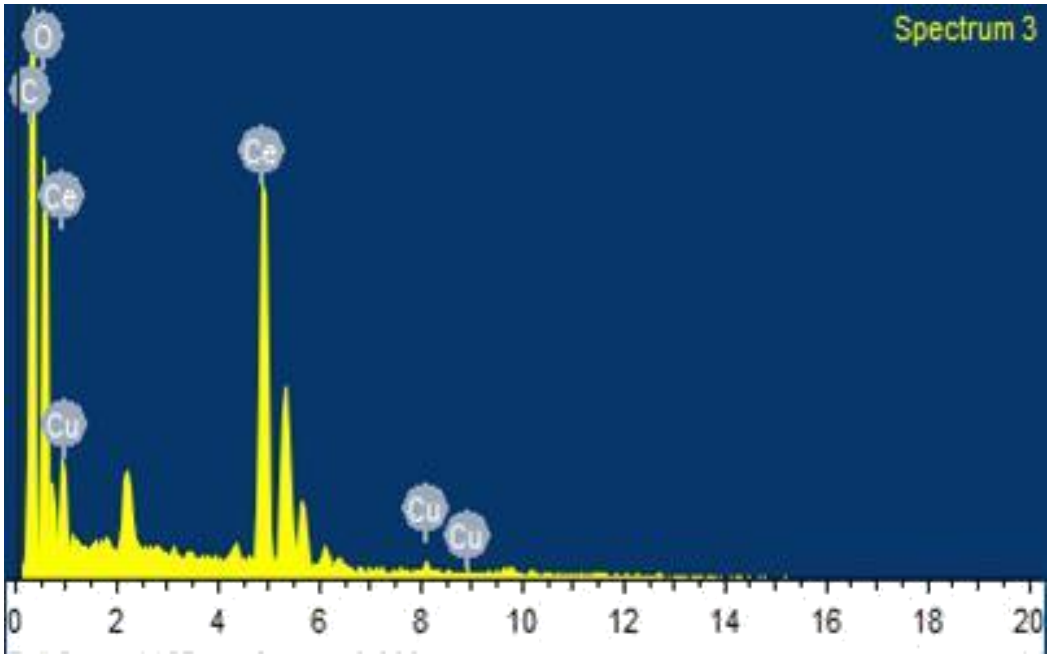

Figure 22 EDS spectrum of Cu doped Ceria

Table 2 Elemental analysis of Cu doped Ceria

Element	App Conc.	Intensity Corrn.	Weight%	Weight% Sigma	Atomic%
C K	28.95	0.4451	44.09	0.87	63.08
O K	17.63	0.3793	31.54	0.83	33.87
Cu K	0.53	0.7867	0.45	0.16	0.12
Ce L	28.00	0.7937	23.92	0.53	2.93
Totals			100.00		

5.4 FTIR Analysis

Fig. 23 and 24 show the FTIR spectrum of as synthesized ZIF-67 and ZIF- 67/CeO_2 catalysts.

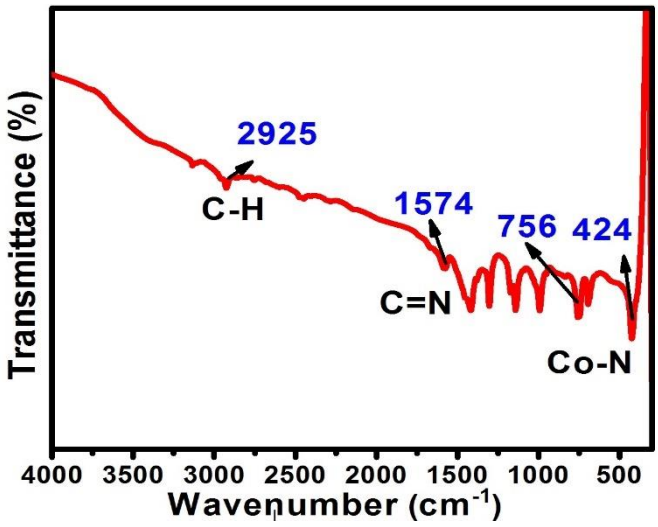

Figure 23 FTIR spectrum of ZIF-67

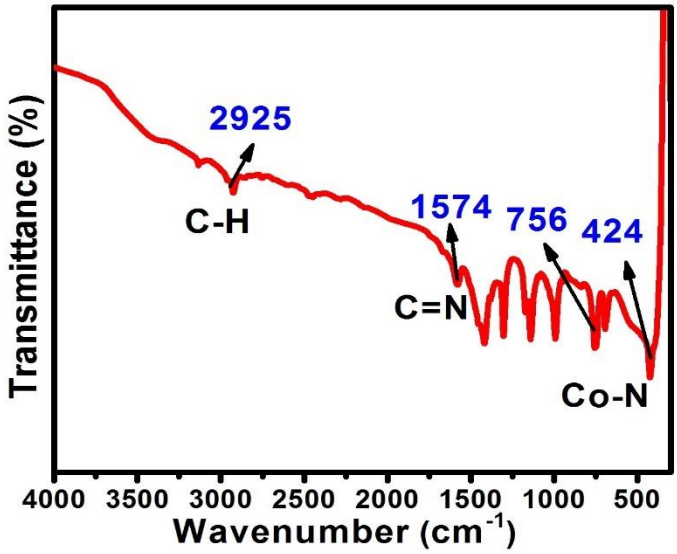

Figure 24 FTIR spectrum ZIF-67/CeO_2

For pure ZIF-67, the strong peaks are obtained at 2925 cm^{-1}, 1574 cm^{-1}, 756 cm^{-1}, and 424 cm^{-1}. The peaks observed at 2925 and 2960 cm^{-1} represent the C-H stretching vibrations of -CH_3 group, while the one at 422 cm^{-1} represents Co-N stretching vibration. The peaks at 1574 cm^{-1} and 756 cm^{-1} correspond to the stretching as well as bending mode vibrations of C=N, which is present in 2-methyl imidazole. Also, the strong peaks around 1000 to 1500 cm^{-1} represent the skeletal vibrations of the imidazole ring present in ZIF-67 [61].

This clearly shows the phase purity of ZIF-67. For ZIF-67/CeO_2, there are no visible peaks present for Ce-O bond. Though all the peaks present display the formation of perfect ZIF-67 crystals.

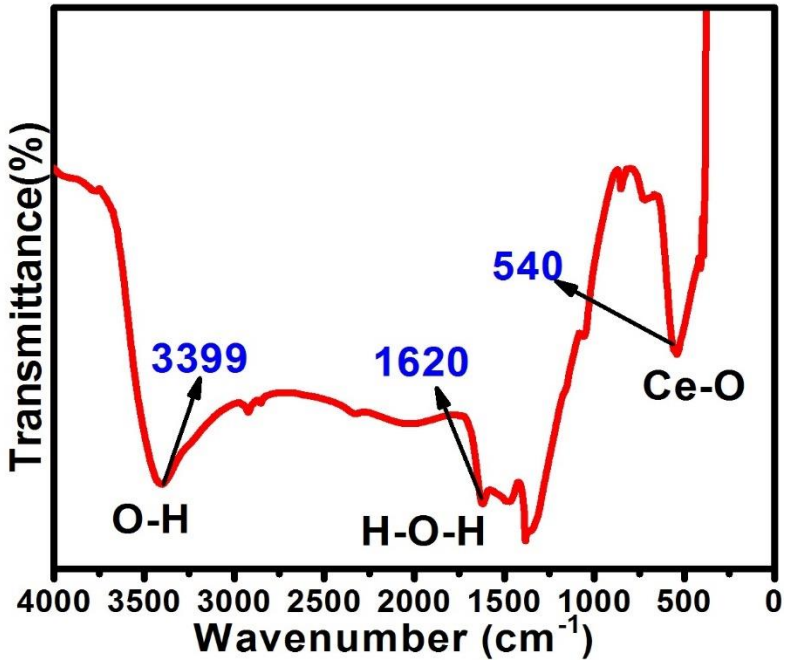

Figure 25 FTIR spectrum of CeO_2

FTIR analysis of the synthesized samples of ceria and Cu doped ceria is shown in the Fig. 25 and 26, respectively. For pure CeO_2, the strong bands can be seen at 3399 cm^{-1}, 1620 cm^{-1}, and 540 cm^{-1}. The broad bands at 3390 cm^{-1} and 1620 cm^{-1} corresponds to the symmetric stretching and bending vibrations of physiosorbed water molecules. Furthermore, the band at 540 cm^{-1} shows the stretching mode of Ce-O bond [62]. For the Cu doped sample, stronger bands are obtained between 1600 to 1300 cm^{-1}, which corresponds to O-C-O stretching band and confirms that more CO_2 was absorbed with the addition of Cu into the sample, as compared to pure ceria. Peaks present around 700 cm^{-1} display the Ce-O-C bending mode vibrations and that is visible in both spectrums. Peak present at 500 cm^{-1} in the doped sample shows stretching vibration of Ce-O bond and verify the formation of cerium oxide without any impurities [63].

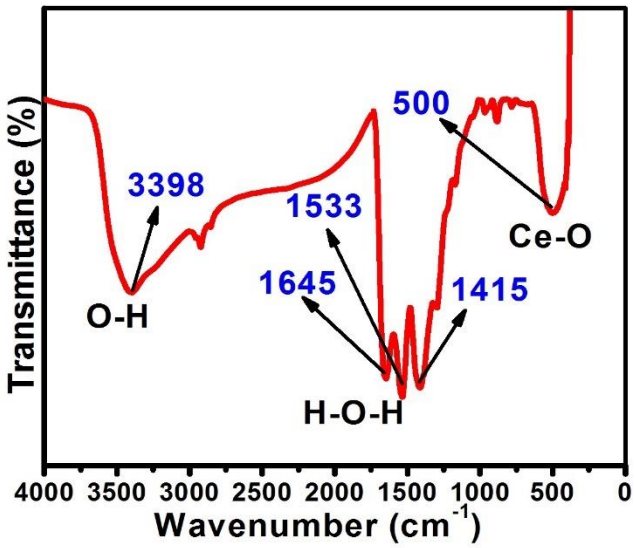

Figure 26 FTIR of Cu doped CeO_2

5.5 TG/DTA Results

Fig. 27 shows the TG and DTA curve for the as-synthesized ZIF-67/CeO_2. We have studied the thermal stability of our prepared samples in air. It is demonstrated from the curve that ZIF67 particles are thermally stable up to temperatures around 300 or 320˚C, in air.

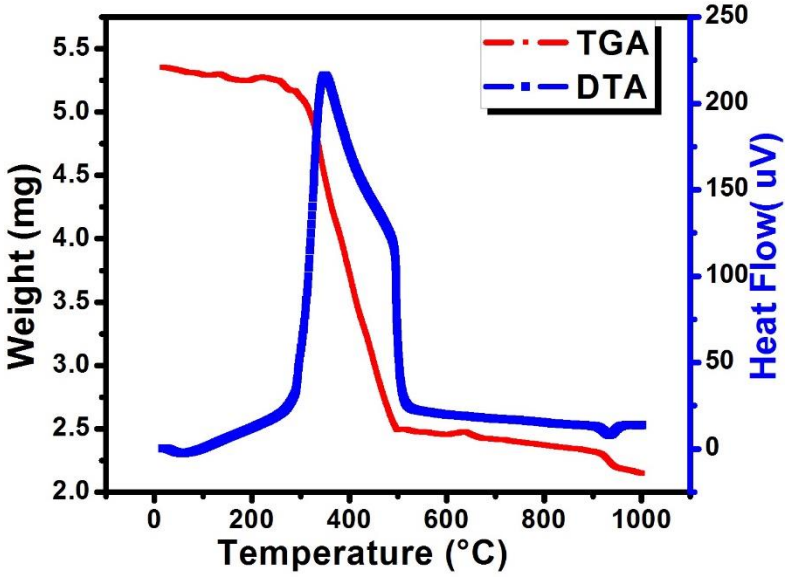

Figure 27 TG/DTA curve of ZIF-67/CeO_2

From the literature, it has been studied that ZIF-67 display a higher thermal stability in vacuum than in air, illustrating its quite sensitive nature towards oxygen at extreme temperatures. Although, its stability still exceeds many other MOFs and metal oxides [35].

The first weight loss peak occurs around 300 ˚C which corresponds to the elimination of guest molecules or any unreacted species and then it follows sudden decomposition. At temperature up to 950 ˚C, the weight remains almost 10% of the original mass [64]. The TG/DTAA curve matches well with the published data for pure ZIF-67. Fig. 28 shows the TG/DTA curves of pure and Cu doped cerium oxide. For pure ceria, a continuous weight loss is observed when it is heated from room temperature to 800 ˚C, which, at first, is due to absorbed water molecules or any unreacted species. The total weight loss observed for CeO_2 sample is almost 20 %. For the Cu doped sample, continuous decomposition starts when it is being heated at room temperature until it becomes stable at 650 ˚C.

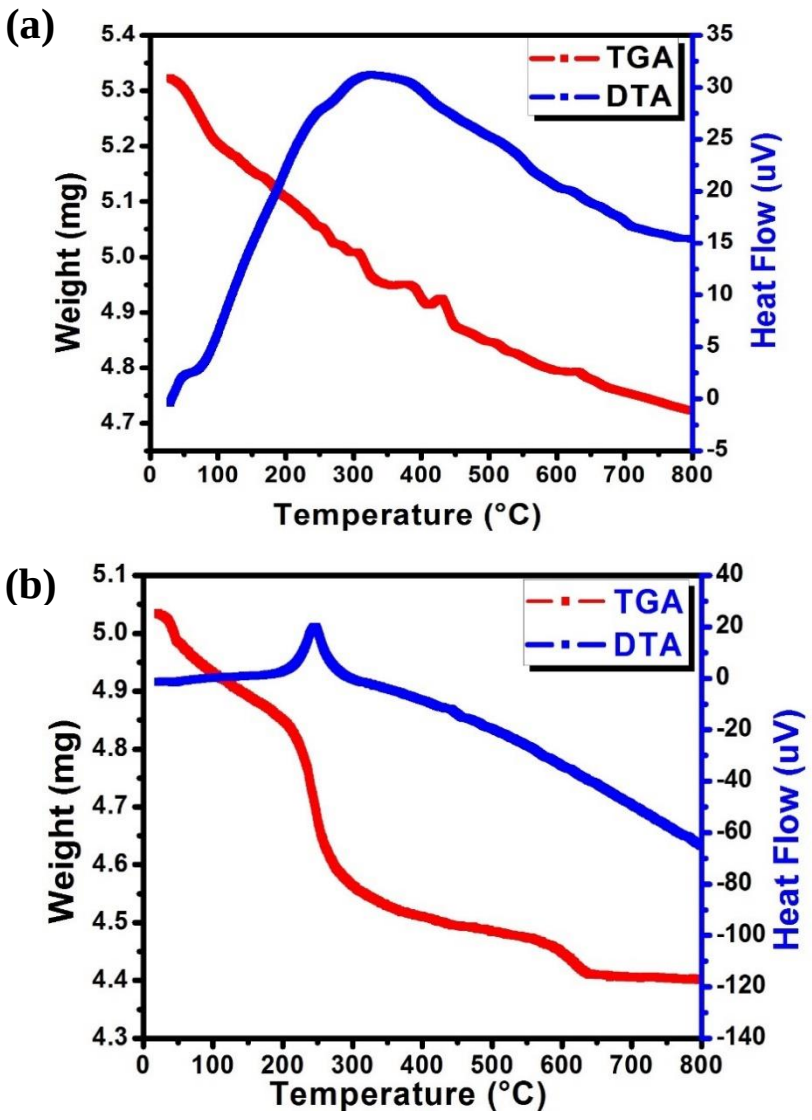

Figure 28 TG/DTA curves of (a) CeO_2, (b) Cu doped CeO_2

Although, both the curves for pure ceria and the doped sample (10 % Cu) exhibit a similar behavior in the start, there is a slight difference in the amount of weight loss at different temperatures, which can be clearly seen form the TGA graphs. Doping of ceria with Cu causes it to be a better thermal conductor, and thus it loses more weight at extreme temperatures in comparison to pure Ceria.

5.6 N_2 Adsorption/Desorption Isotherms

The porosity and specific surface area of the samples which can affect catalytic performance were carefully examined by nitrogen adsorption-desorption isotherm measurements. This is shown in Fig. 29.

For CeO_2 nanoparticles, the N_2 adsorption-desorption isotherms exhibits a type-II adsorption branch reflecting a non-porous character [41]. It is in accordance with the previously published reports. The calculated BET surface area of CeO_2 nanoparticles is 52.5 m^2/g. For ZIF-67 polyhedrons, a type-I N_2 adsorption-desorption without hysteresis was obtained which reflects its microporous nature [34]. Its surface was area measured to be 1085 m^2/g. The pore size distribution of ZIF-67 is also shown where it can be seen that pores with smaller diameter has a larger density in comparison to the pores with larger diameter.

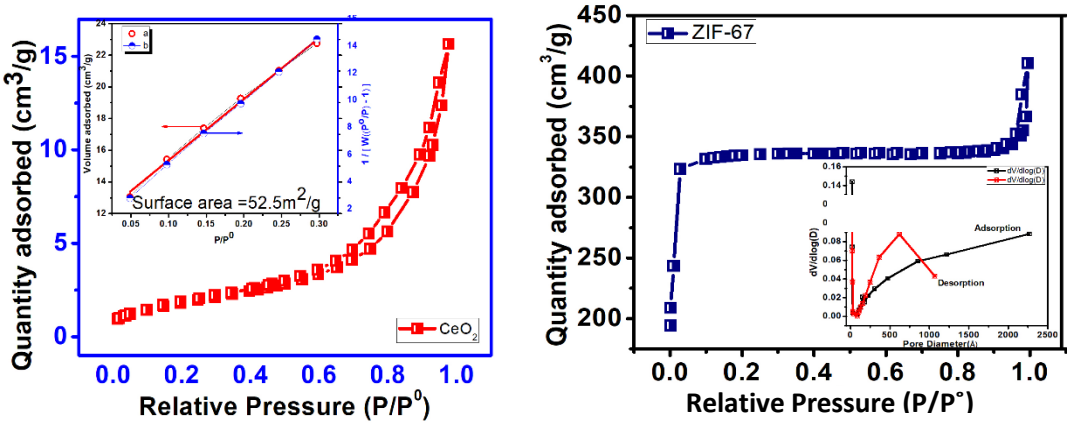

Figure 29 N_2 adsorption-desorption isotherms of CeO_2 and ZIF-67

5.7 XPS Results

XPS is performed for the surface compositional analysis and investigation of the chemical states of the prepared sample. Fig. 30 shows the XPS spectrums that are obtained for the ZIF-67/CeO_2 sample. After curve fitting, the binding energies on Ce 3d spectra conform to the Ce $3d_{3/2}$ and Ce $3d_{5/2}$ spin-orbit states as shown in Fig. 30. The peak at binding energy of 914.9 eV is a character of Ce (IV). In detail, the results obtained from the curve fitting show that the peaks at 880.2, around 884, 900, and 904.0 eV are because of the emissions from Ce^{+3} while all the other peaks i.e. 886.0, 890, 896.3, 898.9 eV are a result of emissions from Ce^{+4}. It matches well with the previously reported work. The ratio of Ce^{3+}/Ce^{4+} can be semi-quantified based on the peak area. The presence of Ce^{+3} may induce more oxygen vacancy defects [41, 65]. The binding energies at 781.8 eV and 796.2 eV are attributed to Co $2p_{3/2}$ and Co $2p_{1/2}$, respectively. The satellite peak at around 786.3 eV is an aspect of Co (II), showing the presence of Co (II) in the product [41]. The O 1s peak are deconvolved into three peaks. The binding energy at 529.5 eV is ascribed to the lattice oxygen of CeO_2, and the one at 531.6 eV can be ascribed to hydroxyl species, defective oxygen and absorbed oxygen. The peak at 533 eV is attributed to absorbed water molecules. XPS signals take into account the chemical state of the surface atoms, and the strong peak at 531 eV suggests that there are a lot of surface hydroxyls in the product and the presence of Ce^{3+} would aid the raise of absorbed oxygen [41]. More precisely, the N1s peak is deconvoluted into three different N species: pyridinic N at 398.3 eV, graphitic N at 398.8 eV. Among them, major species is the pyridinic N that is known to be more active than other N species [66]. The high-resolution spectrum of C 1s is fitted by three peaks at 281.9 282.4, and 284.8.0 eV corresponding to C-C, C=C, and C=N/C-O. These functional groups arise from the decomposition of organic frameworks and notably affect the electronic structure/binding affinity of carbon materials [67].

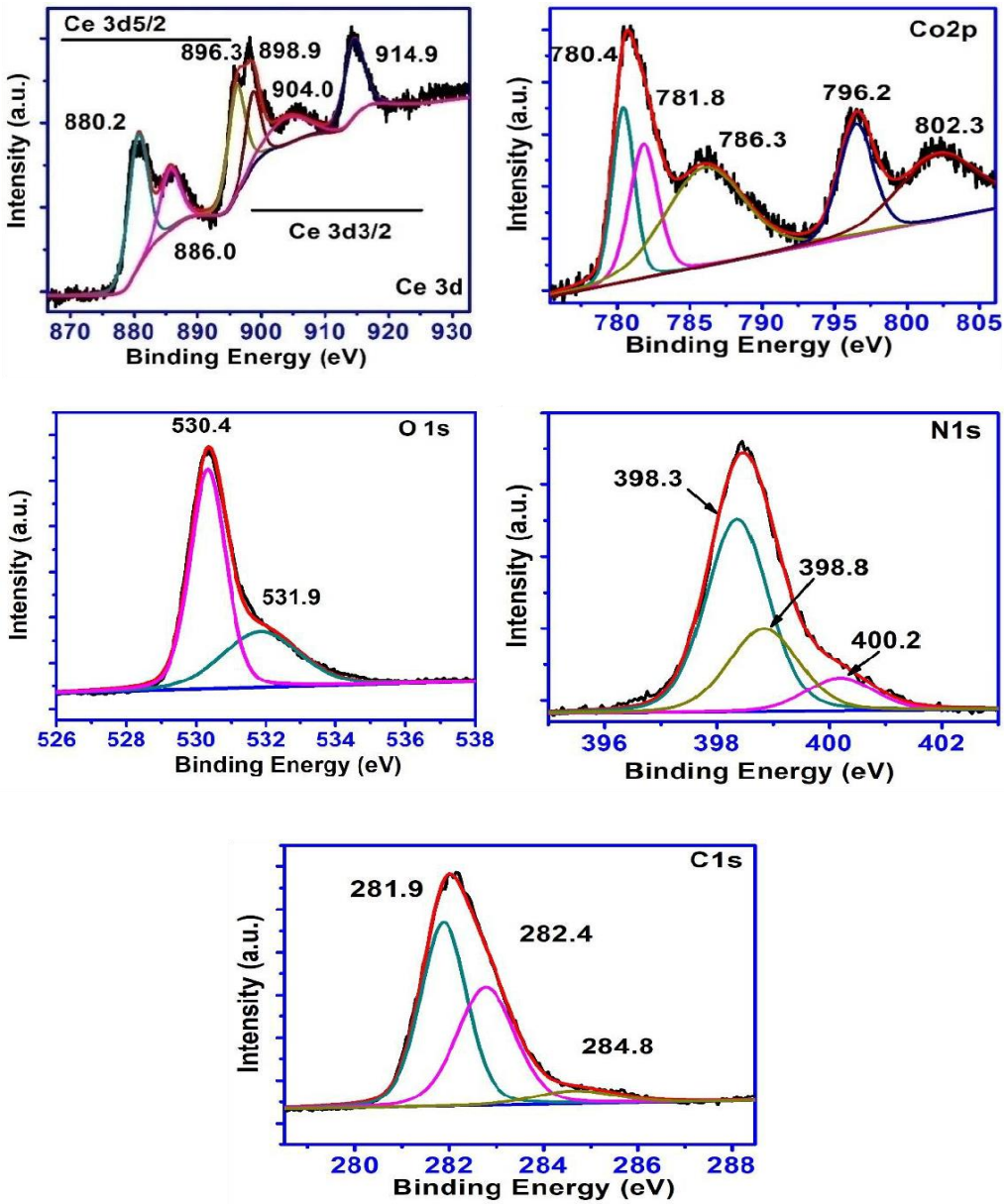

Figure 30 XPS spectra of ZIF-67/CeO_2: Ce 3d, Co 2p, O 1s, N 1s, C 1s

5.8 TPD Results

Fig. 31 shows the NH_3-TPD results obtained for pure ZIF-67, pure CeO_2 and ZIF-67/CeO_2 composite. TPD is done to find out the acidic and basic sites present in the catalyst. For ZIF-67, according to literature it is known that the acidity of ZIF-67 originates from Co (II) and Co (III) species and the basic sites results from N atoms of imidazole ligand present on its surface [68]. In the figure, a desorption peak is obtained at around 250 °C. This shows the moderate acidic strength of ZIF-67 to be used as an active catalyst. For

CeO_2, two desorption peaks are obtained. One at a lower temperature of 100 °C which is attributed to the weak acidic site and with a greater peak area [69]. The peak at a higher temperature of 300 °C shows the presence of moderately strong acidic sites on CeO_2 surface. For the composite sample ZIF-67/CeO_2, less density of weak acidic sites and larger density of moderately strong acid sites are present. This is because of the synergistic impact of ZIF-67 and CeO_2 which results in creating greater acidic sites on the catalyst surface.

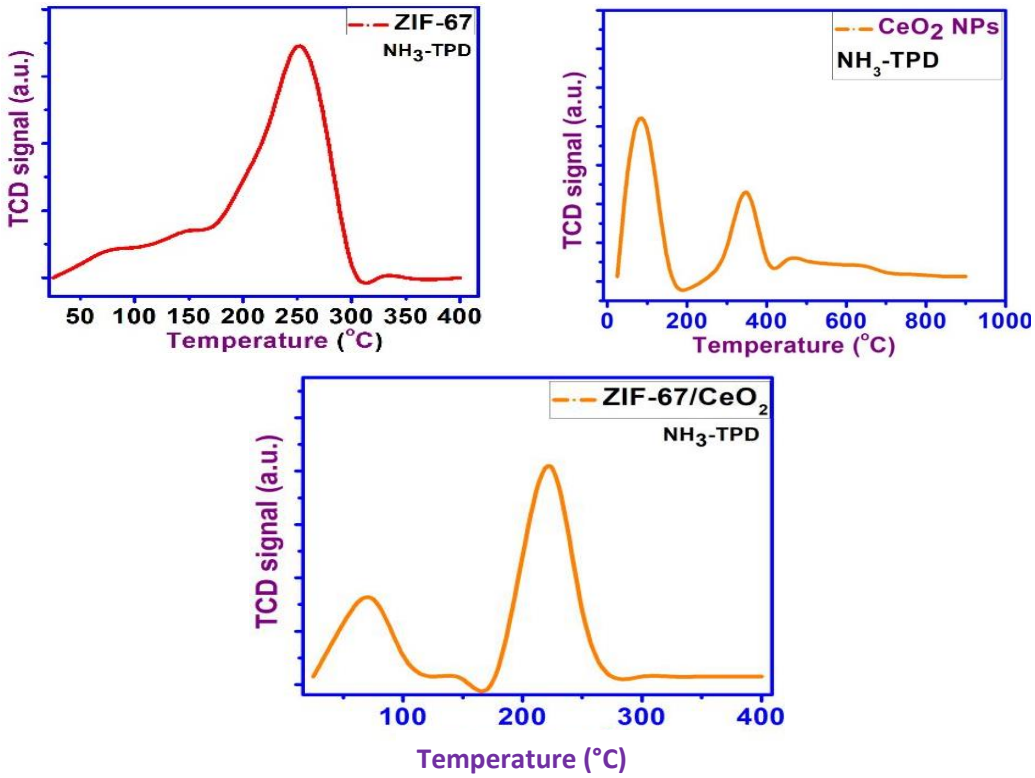

Figure 31 NH_3 – TPD results of ZIF-67, CeO_2 and ZIF-67/CeO_2

5.9 TPR Results

H_2-TPR is done to analyze the reductive behavior of our samples. Fig. 32 shows the TPR result of CeO_2 and ZIF-67/CeO_2. For pure CeO_2, two peaks are obtained at around 400 °C and 800 °C. The lower temperature peak can be ascribed to the capping oxygen present at the surface of ceria whereas the high temperature peak is due to the bulk oxygen present in the sample. These oxygen species are responsible for the hydrogen uptake in H_2-TPR analysis [41]. For the hybrid ZIF-67/CeO_2 sample, three peaks are obtained. The peak around 350 °C is the characteristic peak of ceria which is now shifted to lower temperature

as compared to pure ceria. The peak around 500 °C is the characteristic of ZIF-67 which is ascribed to the presence of N^- species present on its surface and are responsible of hydrogen uptake [68]. The 2nd characteristic peak of ceria is also shifted to lower temperature and it is now at 600 °C with a larger peak area, as compared to pure ceria where it was at 800 °C. This can be explained by the synergistic properties obtained by the formation of a hybrid structure which increases the reducibility and hence the catalytic activity of the catalyst.

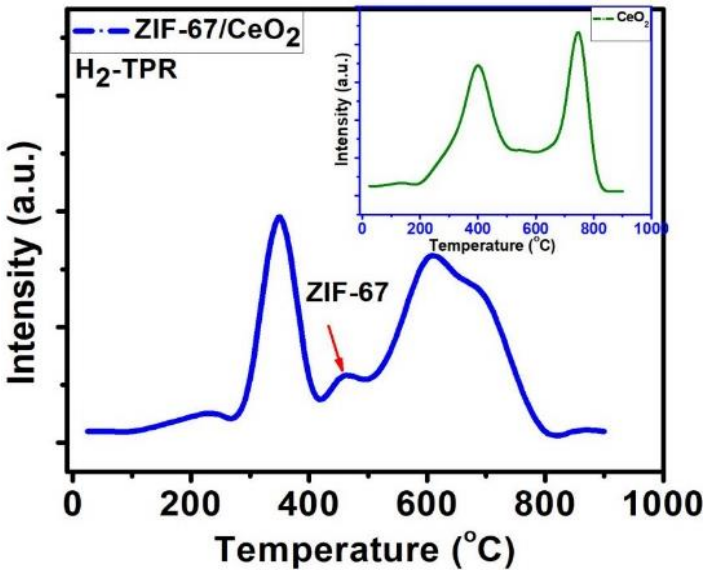

Figure 32 H_2-TPR results of CeO_2 and ZIF-67/CeO_2

5.10 Synthesis of Adipic acid

ZIF-67/CeO_2 was utilized for the synthesis of adipic acid through the oxidation of cyclohexene with H_2O_2. The experiment was performed in a round bottom flask with a reflux condenser. Cyclohexene (25 g) H_2O_2 150 mL, catalyst 1.2 g. 250 mL flask was equipped with reflux condenser and temperature sensor. 1.2 g of the catalyst were taken in flask along with cyclohexene and heated up to 40 °C with subsequent addition of H_2O_2 and stirred at this temperature for 30 min. Further heating was done to 90 °C and kept at that for 12 h. This was done in a water bath. In an oil bath, further heating was done at 110 °C to see the effect of temperature on the product yield. The white crystalline solid was obtained after cooling it down in an ice bath. Fig. 33 shows the FTIR spectrum of the obtained product i.e. adipic acid. The FTIR spectrum of obtained adipic acid display the strong characteristic peak at 1685cm^{-1} which are ascribed to the stretching vibrations

of carboxylic group present in AA. Also, the peak at 2981cm^{-1} display the C-H stretching present in its structure. Other than that, few peaks after 1000 at approximately 1150 and 1300cm^{-1} corresponds to C-O stretching vibrations [70]. This result matches well with the reported work and demonstrates the formation of adipic acid.

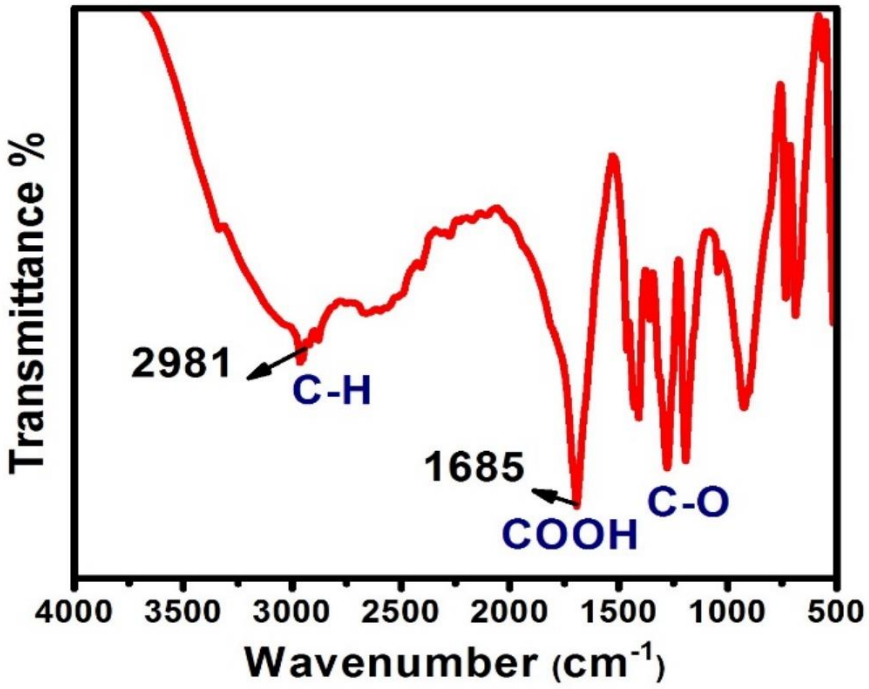

Figure 33 FTIR spectrum of Adipic Acid

5.10.1 Yield Calculation

No. of moles of cyclohexene used:

30.26 mL of cyclohexene was used in the experiment. Using the given volume of 30.26 mL, the molecular weight (82 g/mol), and the density of cyclohexene (0.81 g/ml), the theoretical number of moles of cyclohexene used can be calculated.

$$\text{No. of moles of cyclohexene} = 30.26 \text{ mL cyclohexene} \times \frac{0.81 \text{ g cyclohexene}}{1 \text{ mL cyclohexene}} \times \frac{1 \text{ mol cyclohexene}}{82 \text{ g cyclohexene}}$$

$$= 0.296 \text{ moles cyclohexene}$$

0.296 moles of cyclohexene produce 0.296 moles of adipic acid because cyclohexene has a ratio of 1:1 with adipic acid

Theoretical yield of adipic acid:

The theoretical amount of product obtainable in grams can be computed by multiplying the moles of adipic acid produced to the molecular weight of adipic acid which is 146 g/mol. This is by the knowledge that 0.296 moles adipic acid can be obtained and hence just by converting it to grams, the theoretical yield is known.

$$\text{Theoretical yield} = 0.296 \text{ mol adipic acid} \times \frac{146 \text{ g adipic acid}}{1 \text{ mol adipic acid}}$$

$$= 43.216 \text{ g adipic acid}$$

Percentage yield of adipic acid:

To compute the percentage yield, actual yield which was the yield obtained from the experiment is divided by the theoretical yield which was calculated above, multiplied the whole to 100. The yield obtained from the experiment is 31.1152 grams.

$$\text{Percentage yield} = \frac{\text{Actual yield}}{\text{Theoretical yield}} \times 100\ \%$$

$$= \frac{31.1 \text{ grams}}{43.2 \text{ grams}} \times 100\ \%$$

Percentage yield = 72 %

At temperature 110°C, the yield obtained from the experiment was 33.708 grams.

$$\text{Percentage yield} = \frac{\text{Actual yield}}{\text{Theoretical yield}} \times 100\ \%$$

$$= \frac{33.7 \text{ grams}}{43.2 \text{ grams}} \times 100\ \%$$

Percentage yield = 78 %

The comparison of this work with several previously reported catalysts for this reaction is shown in Table 3.

Table 3 Comparison of this work with other catalysts

Catalysts	Percent yield	Reference
MIL-101	80%	[71]
WO_4/silica gel	84%	[72]
Au/SiO_2	85%	[73]
Ag_2WO_4	57%	[74]
ZIF-67/ CeO_2	72%	This work

5.10.2 Proposed Reaction Mechanism

ZIF67 have been previously reported to be used for several organic transformations but not for this particular reaction where the oxidation of cyclohexene takes place with H_2O_2. The mechanism of previous reaction was explained by the presence of acido-basic sites present on the external surface of ZIF-67 [39, 68]. These active sites are responsible for the catalytic activity of ZIF-67 and their presence is analyzed by the NH_3-TPD results. These species may include OH and NH groups, hydrogenocarbonates, low-coordinated Co atoms, and free N- moieties belonging to the linkers. The proportion of low coordinated Co atoms such as Co III nodes and Co II nodes depends on the number of linkers lost around the exposed Co center [68]. The presence of small amounts of atmospheric moisture may lead to the formation of NH, -OH and hydrogenocarbonate species on the ZIF surface which is shown in Fig. 34. On the other hand, the presence of CeO_2 has its own role in the catalytic activity for this reaction. Ceria has the ability of reversing between two oxidation states i.e. Ce^{+3} and Ce^{+4} and is reported to decompose H_2O_2 to produce molecular oxygen [75].

A proposed mechanism is presented in Fig. 35 based on the presence of active sites present on the catalyst's surface. The oxidation of cyclohexene with H_2O_2, for the production of Adipic acid, goes through several oxidation and hydrolysis steps. The first step is the epoxide formation of cyclohexene, which is accelerated by the rapid decomposition of H_2O_2 by Ce ions present on ceria's surface. It produces more O atoms for the epoxide reaction to take place fast. Secondly, the ring opening of epoxide is proposed to be

accelerated by the presence of Co centers on ZIF's surface. It bonds with oxygen to form CoO or Co_2O_3 compounds and causes the ring opening of epoxide to form a diol. For the ZIF-67/CeO_2 sample, the formation of Adipic acid takes place in less reaction time and at a lower temperature.

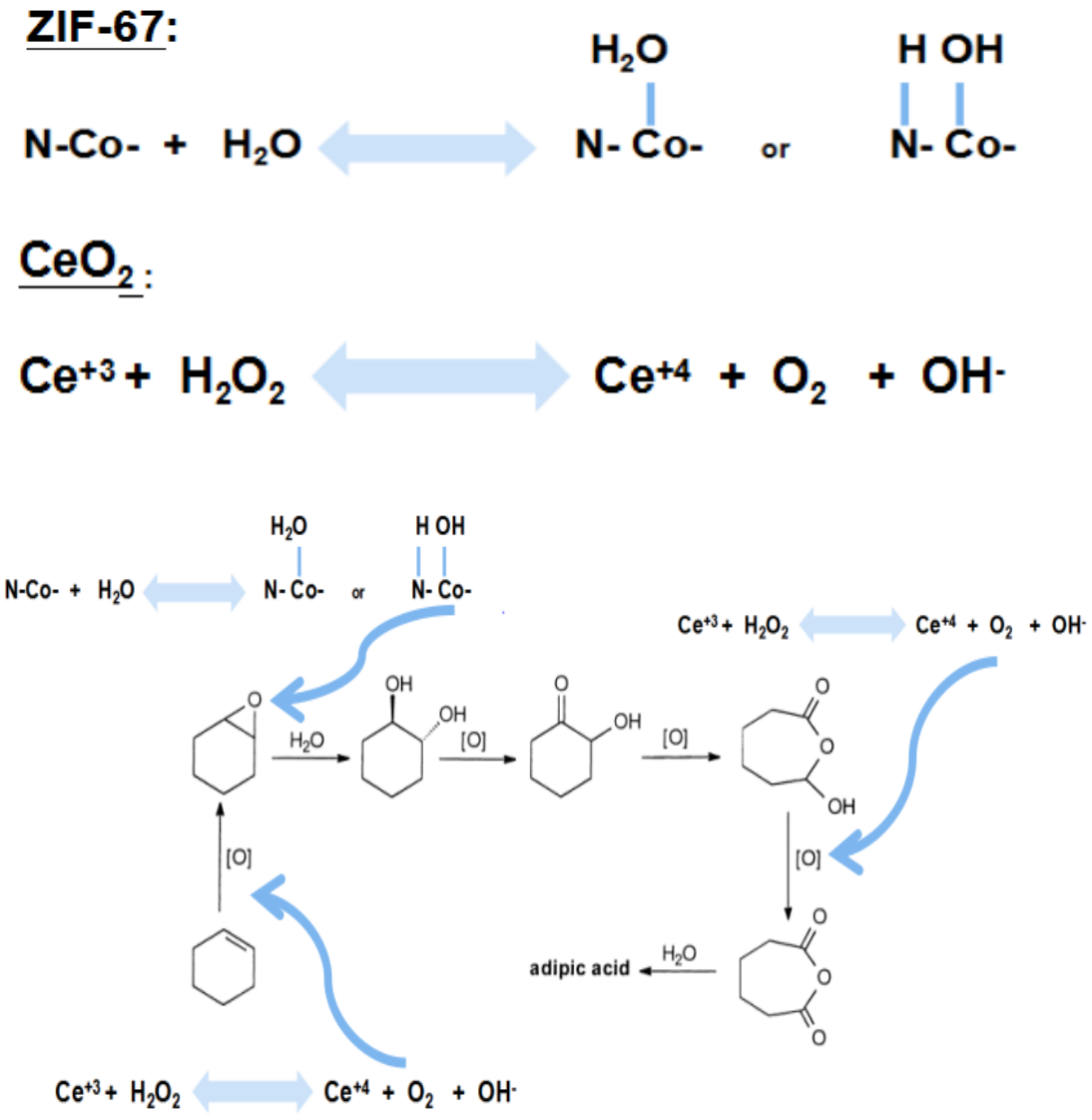

Figure 34 Proposed reaction mechanism of oxidation of cyclohexene with ZIF-67/CeO_2 as a catalyst

Conclusions and Recommendations

6.1 Conclusions

- In conclusion, a facile and cost-effective approach to synthesize a hybrid structure of ceria nanoparticles encapsulated inside an easily assembled MOF i.e. ZIF-67. SEM and TEM results display ceria nanoparticle mounted on the surface as well as embedded inside ZIF-67 structure.
- ZIF-67/CeO_2 composite displayed significant activity for the production of Adipic acid with a percentage yield of 72%.
- The as-prepared metal oxide/ZIF-67 composite comprehend the advantage of mesoporous and molecular sieving manner depicted by the MOF matrix combined with the effective functional characteristics of cerium oxide's nanoparticles.
- Cu doped CeO_2 did not show any activity towards the formation of Adipic acid through oxidation of cyclohexene.

6.2 Recommendations

- This kind of a facile strategy can be extended to encapsulate ceria nanoparticles inside other readily prepared MOFs to develop considerably reactive and recyclable heterogenous catalysts for advanced applications.
- This procedure is suitable to an extensive range of metal/metal oxide nanoparticles as it enables encapsulation of multiple nanoparticles inside MOFs in an un-agglomerated fashion.
- Detailed mechanism of the production of Adipic acid using ZIF-67/CeO_2 catalyst can be studied and evaluated.

References

1. Gupta, C. and N.J.I.M.R. Krishnamurthy, *Extractive metallurgy of rare earths.* 1992. **37**(1): p. 197-248.
2. Rokhlin, L.L., *Magnesium alloys containing rare earth metals: structure and properties*. 2014: Crc Press.
3. Wiberg, E. and N.J.I.c.A.P. Wiberg, *Arnold Frederick Holleman.* 2001.
4. Alessandro, T., *Catalysis by ceria and related materials*. Vol. 2. 2002: World Scientific.
5. Ruiz Puigdollers, A., et al., *Increasing oxide reducibility: the role of metal/oxide interfaces in the formation of oxygen vacancies.* 2017. **7**(10): p. 6493-6513.
6. Wang, X., et al., *Synthesis and shape-dependent catalytic properties of CeO_2 nanocubes and truncated octahedra.* 2012. **14**(22): p. 7579-7582.
7. Xie, X., et al., *Low-temperature oxidation of CO catalyzed by Co_3O_4 nanorods.* 2009. **458**(7239): p. 746.
8. Zhou, K., et al., *Enhanced catalytic activity of ceria nanorods from well-defined reactive crystal planes.* 2005. **229**(1): p. 206-212.
9. Liu, L., et al., *Morphology and Crystal-Plane Effects of Nanoscale Ceria on the Activity of CuO/CeO_2 for NO Reduction by CO.* 2011. **3**(6): p. 978-989.
10. Mai, H.-X., et al., *Shape-selective synthesis and oxygen storage behavior of ceria nanopolyhedra, nanorods, and nanocubes.* 2005. **109**(51): p. 24380-24385.
11. Wang, S., et al., *Morphology control of ceria nanocrystals for catalytic conversion of CO_2 with methanol.* 2013. **5**(12): p. 5582-5588.
12. Choi, M., et al., *Stable single-unit-cell nanosheets of zeolite MFI as active and long-lived catalysts.* 2009. **461**(7261): p. 246.
13. White, R.J., et al., *Supported metal nanoparticles on porous materials. Methods and applications.* 2009. **38**(2): p. 481-494.
14. Reddy, B.M., T.V. Kumar, and N. Durgasri, *New developments in ceria-based mixed oxide synthesis and reactivity in combustion and oxidation reactions*, in *catalysis by ceria and related materials*. 2013, World Scientific. p. 397-464.
15. Zhou, Y., et al., *Resonant Photoemission Observations and DFT Study of s–d Hybridization in Catalytically Active Gold Clusters on Ceria Nanorods.* 2013. **52**(27): p. 6936-6939.

16. Chen, B., et al., *Zeolitic imidazolate framework materials: recent progress in synthesis and applications.* 2014. **2**(40): p. 16811-16831.
17. Fu, Y., et al., *A Novel Non-Enzymatic Electrochemical Hydrogen Peroxide Sensor Based on a Metal-Organic Framework/Carbon Nanofiber Composite.* 2018. **23**(10): p. 2552.
18. Wang, L., et al., *Efficient ferrite/Co/porous carbon microwave absorbing material based on ferrite@ metal–organic framework.* 2017. **326**: p. 945-955.
19. Wang, X., et al., *CeO_2 nanowires self-inserted into porous Co_3O_4 frameworks as high-performance "noble metal free" hetero-catalysts.* 2016. **7**(2): p. 1109-1114.
20. Mao, Y., et al., *General incorporation of diverse components inside metal-organic framework thin films at room temperature.* 2014. **5**: p. 5532.
21. Zanon, A., et al., *1 Zn-doped ZIF-67 as catalyst for the CO_2 fixation into cyclic carbonates.* 2017. **20**: p. 282-291.
22. Wen, Y., et al., *A large-scale continuous-flow process for the production of adipic acid via catalytic oxidation of cyclohexene with H_2O_2.* 2012. **14**(10): p. 2868-2875.
23. Van de Vyver, S., Y.J.C.S. Román-Leshkov, and Technology, *Emerging catalytic processes for the production of adipic acid.* 2013. **3**(6): p. 1465-1479.
24. Acid, A.J.M.R. and U. Consulting: Birmingham, *World Market Outlook and Forecast up to 2027.* 2018.
25. Montzka, S.A., E.J. Dlugokencky, and J.H.J.N. Butler, *Non-CO_2 greenhouse gases and climate change.* 2011. **476**(7358): p. 43.
26. Wu, M., et al., *Catalytic Performance of MgO-Supported Co Catalyst for the Liquid Phase Oxidation of Cyclohexane with Molecular Oxygen.* 2017. **7**(5): p. 155.
27. Deng, Y., et al., *Clean synthesis of adipic acid by direct oxidation of cyclohexene with H_2O_2 over peroxytungstate–organic complex catalysts.* 1999. **1**(6): p. 275-276.
28. Alcañiz-Monge, J., G. Trautwein, and A.J.J.o.M.C.A.C. Garcia-Garcia, *Influence of peroxometallic intermediaries present on polyoxometalates nanoparticles surface on the adipic acid synthesis.* 2014. **394**: p. 211-216.
29. Raj, K., et al., *Biocatalytic production of adipic acid from glucose using engineered Saccharomyces cerevisiae.* 2018. **6**: p. 28-32.

30. Liu, H., et al., *Selective phenol hydrogenation to cyclohexanone over a dual supported Pd–Lewis acid catalyst.* 2009. **326**(5957): p. 1250-1252.
31. Thomas, J.M., et al., *Bimetallic nanocatalysts for the conversion of muconic acid to adipic acid.* 2003(10): p. 1126-1127.
32. Zhao, R., et al., *A highly efficient oxidation of cyclohexane over Au/ZSM-5 molecular sieve catalyst with oxygen as oxidant.* 2004(7): p. 904-905.
33. Scelfo, S., R. Pirone, and N.J.C.C. Russo, *Highly efficient catalysts for the synthesis of adipic acid from cis, cis-muconic acid.* 2016. **84**: p. 98-102.
34. Jiang, Z., et al., *LDH nanocages synthesized with MOF templates and their high performance as supercapacitors.* 2013. **5**(23): p. 11770-11775.
35. Wu, H., et al., *Controlled synthesis of highly stable zeolitic imidazolate framework-67 dodecahedra and their use towards the templated formation of a hollow Co 3 O 4 catalyst for CO oxidation.* 2016. **6**(9): p. 6915-6920.
36. Müller, M., et al., *Loading of MOF-5 with Cu and ZnO nanoparticles by gas-phase infiltration with organometallic precursors: properties of Cu/ZnO@ MOF-5 as catalyst for methanol synthesis.* 2008. **20**(14): p. 4576-4587.
37. Müller, M., et al., *Nanometer-sized titania hosted inside MOF-5.* 2009(1): p. 119-121.
38. Lin, K.-Y.A. and H.-A.J.J.o.t.T.I.o.C.E. Chang, *Zeolitic Imidazole Framework-67 (ZIF-67) as a heterogeneous catalyst to activate peroxymonosulfate for degradation of Rhodamine B in water.* 2015. **53**: p. 40-45.
39. Mousavi, B., et al., *Zeolitic imidazole framework-67 as an efficient heterogeneous catalyst for the conversion of CO_2 to cyclic carbonates.* 2016. **40**(6): p. 5170-5176.
40. Yang, H., et al., *Doping copper into ZIF-67 for enhancing gas uptake capacity and visible-light-driven photocatalytic degradation of organic dye.* 2012. **22**(41): p. 21849-21851.
41. Li, Z., et al., *Hollow CeO_2 dodecahedrons: one-step template synthesis and enhanced catalytic performance.* 2016. **6**(65): p. 60975-60982.
42. Yang, D., et al., *Synthesis of one-dimensional $Ce_{1-x}Y_xO_{2-x/2}$ ($0 \leq x \leq 1$) solid solutions and their catalytic properties: the role of oxygen vacancies.* 2010. **114**(19): p. 8926-8932.

43. Li, T., et al., *Enhanced catalytic performance of assembled ceria necklace nanowires by Ni doping.* 2011. **47**(21): p. 6060-6062.
44. Kundakovic, L. and M.J.J.o.C. Flytzani-Stephanopoulos, *Cu-and Ag-modified cerium oxide catalysts for methane oxidation.* 1998. **179**(1): p. 203-221.
45. Knauth, P., et al., *Emf measurements on nanocrystalline copper-doped ceria.* 1998. **140**(2): p. 295-299.
46. Terribile, D., et al., *Catalytic combustion of hydrocarbons with Mn and Cu-doped ceria– zirconia solid solutions.* 1999. **47**(1-4): p. 133-140.
47. Tschöpe, A., M.L. Trudeau, and J.Y.J.T.J.o.P.C.B. Ying, *Redox properties of nanocrystalline Cu-doped cerium oxide studied by isothermal gravimetric analysis and X-ray photoelectron spectroscopy.* 1999. **103**(42): p. 8858-8863.
48. Li, Y., Q. Fu, and M.J.A.C.B.E. Flytzani-Stephanopoulos, *Low-temperature water-gas shift reaction over Cu-and Ni-loaded cerium oxide catalysts.* 2000. **27**(3): p. 179-191.
49. Wang, X., et al., *Unusual Physical and Chemical Properties of Cu in Ce_{1-x} Cu_xO_2 Oxides.* 2005. **109**(42): p. 19595-19603.
50. Yang, F., et al., *Copper doped ceria nanospheres: surface defects promoted catalytic activity and a versatile approach.* 2014. **2**(16): p. 5662-5667.
51. Lin, M., et al., *Hydrothermal synthesis of CeO_2 nanocrystals: Ostwald ripening or oriented attachment?* 2012. **12**(6): p. 3296-3303.
52. Cullity, B., *Elements of X-ray Diffraction, Department of Metallurgical Engineering and Materials Science, University of Notre Dame*. 1978, Addison-Wesley.
53. Goldstein, J.I., et al., *Scanning electron microscopy and X-ray microanalysis*. 2017: Springer.
54. Williams, D.B. and C.B. Carter, *The transmission electron microscope*, in *Transmission electron microscopy*. 1996, Springer. p. 3-17.
55. Bell, D. and A. Garratt-Reed, *Energy dispersive X-ray analysis in the electron microscope*. 2003: Garland Science.
56. Smith, B.C., *Fundamentals of Fourier transform infrared spectroscopy*. 2011: CRC press.
57. Stoyanova, E., *Setup of a Fourier Transform Infrared Spectrometer.* 2016.

58. Coats, A. and J.J.A. Redfern, *Thermogravimetric analysis. A review.* 1963. **88**(1053): p. 906-924.
59. Hurst, N.W., et al., *Temperature programmed reduction.* 1982. **24**(2): p. 233-309.
60. Barr, T.L., *Modern ESCA: The Principles and Practice of X-Ray Photoelectron Spectroscopy*. 1994: CRC press.
61. Wu, Z., et al., *Facile synthesis and excellent electrochemical performance of reduced graphene oxide–Co_3O_4 yolk-shell nanocages as a catalyst for oxygen evolution reaction.* 2016. **4**(35): p. 13534-13542.
62. Chen, W., F. Li, and J.J.M.L. Yu, *Combustion synthesis and characterization of nanocrystalline CeO_2-based powders via ethylene glycol–nitrate process.* 2006. **60**(1): p. 57-62.
63. Kumar, K.S. and N.V.J.A.J.o.C. Jaya, *Synthesis and Characterization of Pure and Sn-Doped CeO_2 Nanoparticles.* 2013. **25**(11).
64. Yang, X., et al., *Novel Co_3O_4 nanoparticles/nitrogen-doped carbon composites with extraordinary catalytic activity for oxygen evolution reaction (OER).* 2018. **10**(1): p. 15.
65. Xu, Q., et al., *Efficient removal of formaldehyde by nanosized gold on well-defined CeO_2 nanorods at room temperature.* 2014. **48**(16): p. 9702-9708.
66. Park, K.S., et al., *Characterization of Zeolitic Imidazolate Framework-Derived Polyhedral Carbonaceous Material and Its Application to Electrocatalyst for Oxygen Reduction Reaction.* 2016. **11**: p. 9295-9306.
67. Ma, G., et al., *Metal-organic framework-derived $Co_{0.85}Se$ nanoparticles in N-doped carbon as a high-rate and long-lifespan anode material for potassium ion batteries.* 2018. **10**: p. 241-248.
68. Kurruppathparambil, R.R, et al., *A room temperature synthesizable and environmental friendly heterogeneous ZIF-67 catalyst for the solvent less and co-catalyst free synthesis of cyclic carbonates*. 2016. **182:** p. 562-569.
69. Lee, H., et al., *Conversion of acetic acid from the catalytic pyrolysis of xylan over CeO_2.* 2016. **16**(5): p. 4480-4482
70. Zhou, X., et al., *Weldability modification of conductive silver adhesion for piezoelectric composite material by co-doping of metal material and oxide material.* 2019. **517**: p. 237-246.

71. Saedi, Z., et al., *MIL-101 metal–organic framework: A highly efficient heterogeneous catalyst for oxidative cleavage of alkenes with H_2O_2.* 2012. **17**: p. 18-22.
72. Vafaeezadeh, M. and M.M.J.C.C. Hashemi, *Simple and green oxidation of cyclohexene to adipic acid with an efficient and durable silica-functionalized ammonium tungstate catalyst.* 2014. **43**: p. 169-172.
73. Donoeva, B.G., D.S. Ovoshchnikov, and V.B.J.A.C. Golovko, *Establishing a Au nanoparticle size effect in the oxidation of cyclohexene using gradually changing Au catalysts.* 2013. **3**(12): p. 2986-2991.
74. Vafaeezadeh, M. and M.M.J.R.A. Hashemi, *One pot oxidative cleavage of cyclohexene to adipic acid using silver tungstate nano-rods in a Brønsted acidic ionic liquid.* 2015. **5**(40): p. 31298-31302.
75. Wang, X., et al., *Clean synthesis of $Cu_2O@CeO_2$ core@ shell nanocubes with highly active interface.* 2015. **7**(1): p. e158.